The influence of confining stress and preexisting damage on strain localization in fluid-saturated crystalline rocks in the upper crust

Jessica McBeck<sup>1</sup>, Benoit Cordonnier<sup>2</sup>, Yehuda Ben-Zion<sup>3</sup>, and François Renard<sup>1</sup>

May 2, 2023

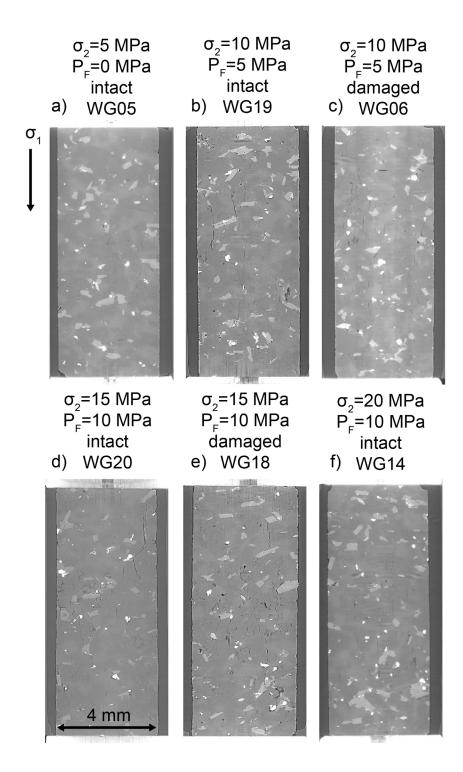
#### Abstract

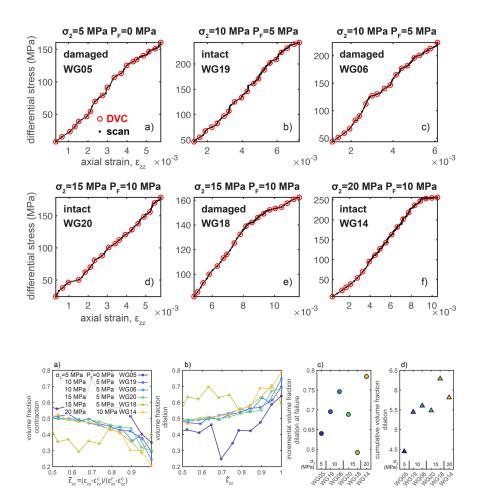
The spatial organization of deformation may provide key information about the timing of catastrophic failure in the brittle regime. In an ideal homogenous system, deformation may continually localize toward macroscopic failure, and so increasing localization unambiguously signals approaching failure. However, recent analyses demonstrate that deformation, including low magnitude seismicity, and fractures and strain in triaxial compression experiments, experience temporary phases of delocalization superposed on an overall trend of localization toward large failure events. To constrain the conditions that promote delocalization, we perform a series of X-ray tomography experiments at varying confining stresses (5-20 MPa) and fluid pressures (zero to 10 MPa) on Westerly granite cores with varying amounts of preexisting damage. We track the spatial distribution of the strain events with the highest magnitudes of the population within a given time step. The results show that larger confining stress promotes more dilation, and promotes greater localization of the high strain events approaching macroscopic failure. In contrast, greater amounts of preexisting damage promote delocalization. Importantly, the dilative strain experiences more systematic localization than the shear strain, and so may provide more reliable information about the timing of catastrophic failure than the shear strain.

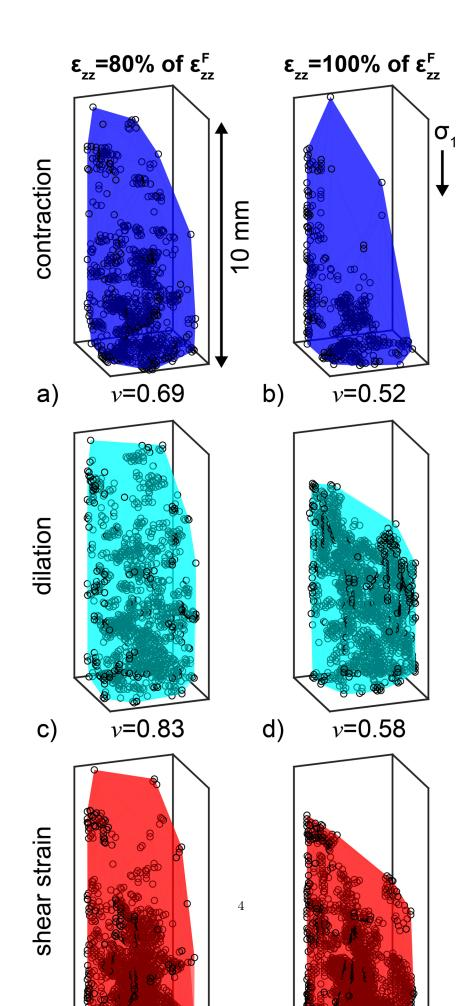
<sup>&</sup>lt;sup>1</sup>University of Oslo

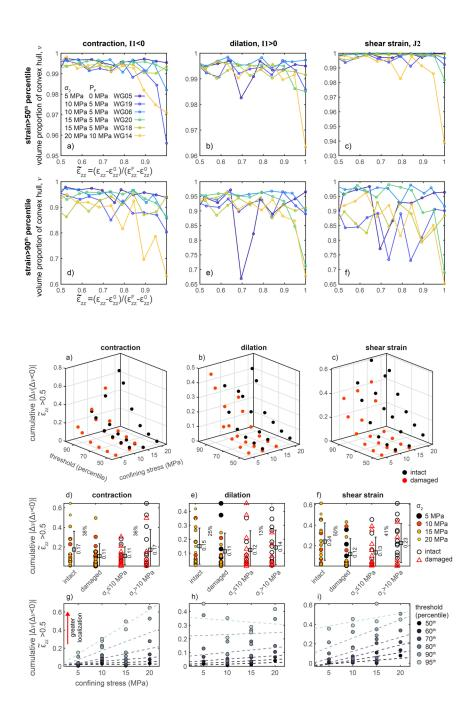
<sup>&</sup>lt;sup>2</sup>ESRF

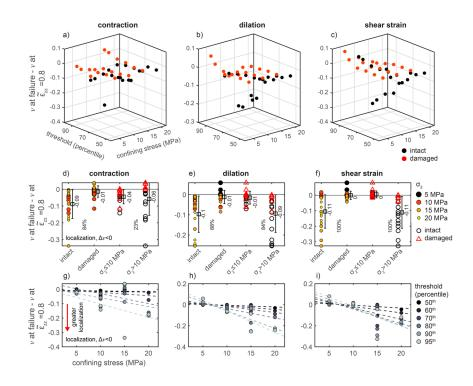
<sup>&</sup>lt;sup>3</sup>University of Southern California

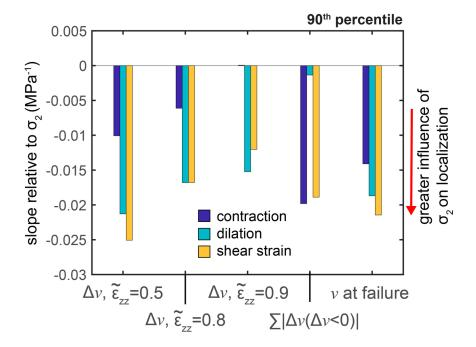


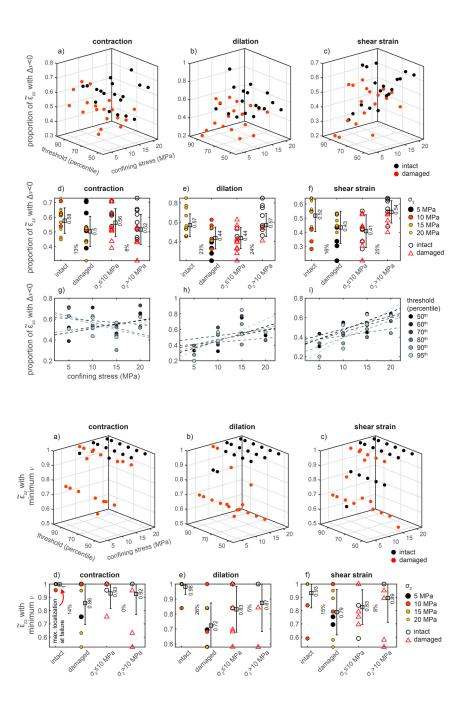


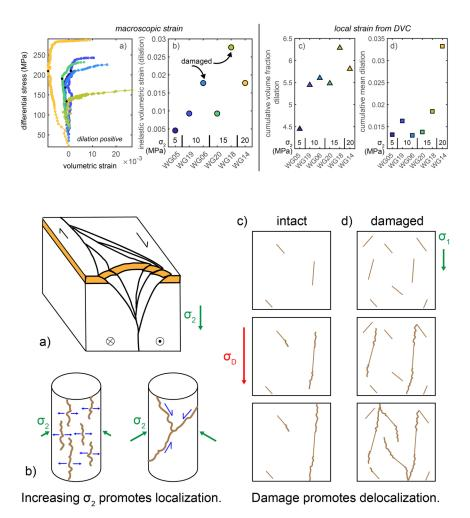












- 1 The influence of confining stress and preexisting damage on strain
- 2 localization in fluid-saturated crystalline rocks in the upper crust
- 3 Jessica McBeck<sup>1</sup>, Benoît Cordonnier<sup>2</sup>, Yehuda Ben-Zion<sup>3</sup>, François Renard<sup>1,4</sup>
- <sup>4</sup> Njord Centre, Departments of Physics and Geosciences, University of Oslo, Oslo, Norway.
- 5 <sup>2</sup>European Synchrotron Radiation Facility, Grenoble, France.
- 6 <sup>3</sup>Department of Earth Sciences and Southern California Earthquake Center, University of
- 7 Southern California, Los Angeles, CA, USA.
- <sup>4</sup>Université Grenoble Alpes, Université Savoie Mont Blanc, Université Gustave Eiffel,
- 9 CNRS, IRD, ISTerre, 38000 Grenoble, France.
- 10 Corresponding author: Jessica McBeck (j.a.mcbeck@geo.uio.no)
- 11 Key Points:
- Digital volume correlation of X-ray tomograms reveals strain localization in triaxial compression experiments.
- Larger confining stress promotes localization approaching macroscopic failure.
- More preexisting damage promotes episodes of delocalization.

### **Abstract**

16

33

48

49

50 51

52

53

54

55

56

57

58

- 17 The spatial organization of deformation may provide key information about the timing of
- 18 catastrophic failure in the brittle regime. In an ideal homogenous system, deformation may
- 19 continually localize toward macroscopic failure, and so increasing localization
- 20 unambiguously signals approaching failure. However, recent analyses demonstrate that
- 21 deformation, including low magnitude seismicity, and fractures and strain in triaxial
- 22 compression experiments, experience temporary phases of delocalization superposed on an
- 23 overall trend of localization toward large failure events. To constrain the conditions that
- 24 promote delocalization, we perform a series of X-ray tomography experiments at varying
- 25 confining stresses (5-20 MPa) and fluid pressures (zero to 10 MPa) on Westerly granite cores
- with varying amounts of preexisting damage. We track the spatial distribution of the strain 26
- 27 events with the highest magnitudes of the population within a given time step. The results
- 28 show that larger confining stress promotes more dilation, and promotes greater localization of
- 29 the high strain events approaching macroscopic failure. In contrast, greater amounts of
- 30 preexisting damage promote delocalization. Importantly, the dilative strain experiences more
- 31 systematic localization than the shear strain, and so may provide more reliable information
- about the timing of catastrophic failure than the shear strain. 32

## **Plain Language Summary**

- 34 The ability of deformation, such as fractures and strain, to spatially cluster or localize
- 35 produces a wide range of geologic features on Earth, such as crustal fault networks and plate
- tectonics. Previous work demonstrates that deformation can evolve toward more localized 36
- 37 distributions. However, recent analyses show that deformation can temporarily decrease in
- localization. These decreases in localization complicate efforts to use the spatial organization 38
- 39 of seismicity, for example, as a precursor of approaching large earthquakes. The factors that
- 40 promote phases of delocalization remain unconstrained. Here, we perform a series of
- 41 experiments to identify the factors that control the delocalization of local strain events within
- 42 low porosity, Westerly granite rock cores. We find that both the confining stress, indicative
- 43 of depth within the crust, and the amount of preexisting damage of the rock cores control the
- 44 amount of localization that the strain events experience, and the phases of delocalization.
- 45 Increasing confining stress produces more localization of the high strain events. More
- 46 preexisting damage produces more delocalization.
- 47 **Key words**: localization, strain, triaxial compression, confining stress, dilation, granite

### 1 Introduction

The localization of strain along fractures, faults, and shear zones is a fundamental phenomenon of rock deformation (e.g., Rudnicki & Rice, 1975; Lockner et al., 1991; Satoh et al., 1996; Benson et al., 2007; Lyakhovsky et al., 2011; Ben-Zion & Zaliapin, 2019). The ability of deformation to localize from the micrometer- to kilometer-scale allowed the Earth's crust to partition into different volumes, and thus is responsible for plate tectonics (e.g., Gueydan et al., 2014; Mulyukova & Bercovici, 2019). Monitoring the localization of deformation may also be useful for recognizing the development of a preparation phase that leads to catastrophic failure in the upper crust, such as large magnitude earthquakes. In particular, machine learning analyses indicate that tracking the distance between fractures in triaxial compression experiments can help successfully predict the timing of catastrophic failure (McBeck et al., 2020b). Similarly, recent observations show that low magnitude seismicity localized in the final two to three years preceding several M>7 earthquakes in

- 59 60
- Southern and Baja California (Ben-Zion & Zaliapin, 2020). However, for some earthquakes, 61
- 62 the seismicity periodically decreased in localization, or delocalized, in the several months

preceding the earthquake. These phases of delocalization obscure the relationship between macroscopic failure and localization, and thereby complicate efforts to forecast the timing of an impending large earthquake using the spatial distribution of seismicity. The factors that control whether a rock or crustal volume may experience phases of delocalization remain largely unconstrained.

To help constrain these factors, we perform a series of X-ray synchrotron tomography triaxial compression experiments and track the localization of the local three-dimensional strains calculated from digital volume correlation. To assess the influence of confining stress and effective stress on strain localization, we systematically change the confining stress from 5 MPa to 20 MPa, and fluid pressure from zero to 10 MPa in the experiments. To assess the influence of preexisting heterogeneities on localization, we introduce a network of preexisting fractures and weaknesses into several of the rock cores by thermal treatment. This set of experiments thus allows comparison of the localization of the strain events in relatively intact and damaged rocks, and in systems with lower and higher confining stress.

## 2 Methods

 2.1. X-ray tomography triaxial compression experiments

We performed six triaxial compression experiments at beamline ID19 at the European Synchrotron Radiation Facility. We used 10 mm tall and 4 mm diameter cylinders of Westerly granite, which is a low-porosity crystalline rock dominated by quartz, feldspar, and biotite. The initial porosity is lower than 1%.

We imposed a constant confining stress in each experiment (5-20 MPa), and constant pore fluid pressure (0-10 MPa) (**Figure 1**) with the Hades triaxial compression apparatus (Renard et al., 2016). We varied the confining stress and fluid pressure so that five of the experiments experienced the same effective stress, confining stress minus fluid pressure ( $P_e$ =5 MPa), and one of the experiments experienced  $P_e$ =10 MPa. **Table** S1 lists all the symbols and notations used here. We increased the axial stress in steps of 0.5-5 MPa until the rock failed with a stress drop, with smaller steps closer to failure. After each increase in axial stress, we acquired a X-ray tomogram within one and half minutes while the core was inside the deformation apparatus.

We deformed intact and heat-treated, or damaged, Westerly granite cores. The crack density produced by thermal heating depends on the temperature, differences in the thermal expansion of the minerals, initial porosity, and the grain size (e.g., Fredrich & Wong, 1986). Heating granite to temperatures above 600°C produces significant increases in the crack density and porosity, and decreases in the P-wave speed and uniaxial compressive strength (Griffiths et al., 2017). We heated the cores with an initial heating rate of 4°C/minute from room temperature to 650°C in an oven, and then for five hours at 650°C, and then with a cooling rate of 4°C/minute to room temperature. This heating procedure causes the damaged rock cores to fail at lower differential stresses than the intact rock cores for the same confining stress and effective stress conditions. We performed all the experiments at ambient room temperature in the range 22-24°C. For the experiments that include fluid pressure, we saturated the granite cores in deionized water in a vacuum chamber for two weeks before the experiment.

Following each experiment, we reconstructed the acquired radiographs into three-dimensional volumes. The three-dimensional volumes, or tomograms, are 1600x1600x1600 voxels, and each voxel side length is  $6.5~\mu m$ . The spatial resolution of the tomograms is

### manuscript submitted to JGR Solid Earth

within two to three voxel side lengths. During reconstruction, we applied methods to remove acquisition noise. We then reduced the remaining noise in the reconstructed, three-dimensional data using the software Avizo3D<sup>TM</sup>, such as a non-local means filter (Buades et al., 2005). We calculate the macroscopic axial strain done on the rock cores,  $\varepsilon_{zz}$ , using the height of the rock core identified in each tomogram. Consequently, the spatial resolution and quality of the tomogram influence the calculated  $\varepsilon_{zz}$ .

In one of the experiments on a damaged core (WG18), a system-spanning, horizontal fracture developed as the core was inserted into the deformation apparatus (**Figure S1**). With increasing axial stress, this fracture closed, and other fractures propagated throughout the core. This large preexisting fracture caused this core to fail at a lower differential stress, and to accumulate more  $\varepsilon_{zz}$  preceding macroscopic failure than expected, and than the other experiments. This experiment thus represents an endmember of rock deformation within a preexisting highly fractured system.

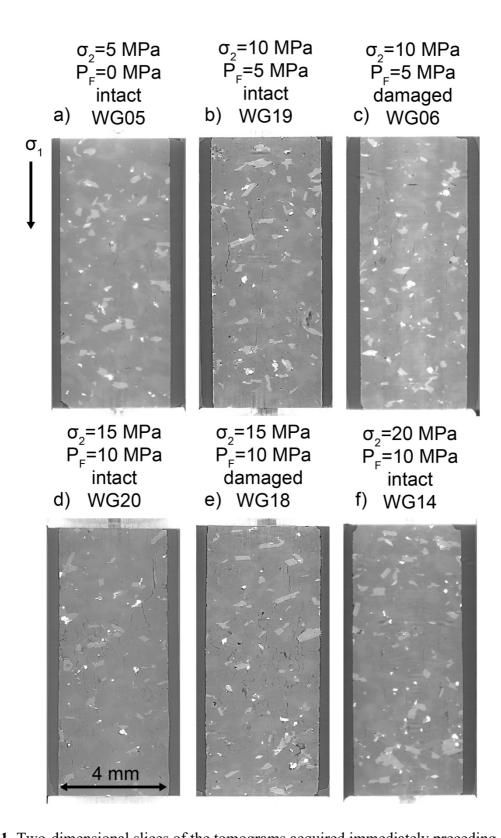


**Figure 1**. Two-dimensional slices of the tomograms acquired immediately preceding macroscopic failure in the six experiments. Minerals with larger densities, such as oxides and biotite, have larger gray-scale values in the tomograms (lighter gray and white regions), than minerals with lower densities, such as quartz and feldspar (darker gray). The fractures have lower gray-scale values (dark gray and black). The applied confining stress,  $\sigma_2$ , and fluid pressure,  $P_F$ , and whether the rock core was damaged or intact are listed above each slice.

## 2.2. Digital volume correlation analysis

To calculate the local three-dimensional strain fields, we used the software TomoWarp2 (Tudisco et al., 2017). Digital volume correlation analyses search for similar patterns of voxels in pairs of three-dimensional images and then calculate the displacement vector that maps a pattern in one image to a pattern in another image (e.g., Charalampidou et al., 2011). In TomoWarp2, the node spacing and correlation window size determine the spatial resolution and the size of the volume used to identify similar patterns of voxels, respectively. Calculations with a node spacing of 20 voxels (0.13 mm) and correlation window size of 10 voxels (65  $\mu$ m) produce an acceptable spatial resolution and reasonable levels of signal to noise (McBeck et al., 2018).

To identify the tomograms used in the digital volume correlation analysis, we divide each experiment into 20 equal increments of the macroscopic axial strain,  $\varepsilon_{zz}$ , and then identify the tomograms with the closest  $\varepsilon_{zz}$  to the specified increments (Figure 2), following our previous analyses (e.g., McBeck et al., 2018). We then use these pairs of tomograms to perform 19 digital volume correlation calculations for each experiment. The reported strain tensors are thus the local, incremental strains done between each tomogram acquisition, and not the total cumulative strain over the entire experiment. To quantify the localization of the volumetric and deviatoric components of the strain field, we calculate the divergence, I1, (volumetric strain, contractive, I1 < 0, and dilative, I1 > 0) and the second invariant of the deviatoric strain tensor, 12, (deviatoric strain, shear) from the incremental displacement fields. In previous analyses, we used the curl of the displacement field to characterize the shear strain, following the technique of the geodetic community (McBeck et al., 2019, 2020c). However, recent machine learning analyses suggest that 12 may provide more information about the timing of fault reactivation and macroscopic failure in strike-slip fault systems than the curl of the displacement field (McBeck et al 2022a). We also use 12 to characterize the shear strain because it determines the maximum distortion criterion, or von Mises yield criterion. Because each tomogram captures regions outside the rock core, such as the jacket and deformation apparatus, we remove the portion of the calculated strain field that is outside the rock core.

128

129

130

131

132

133

134

135

136

137

138

139

140

141142

143144

145

146

147

148

149150

151

152

153

154

155

156

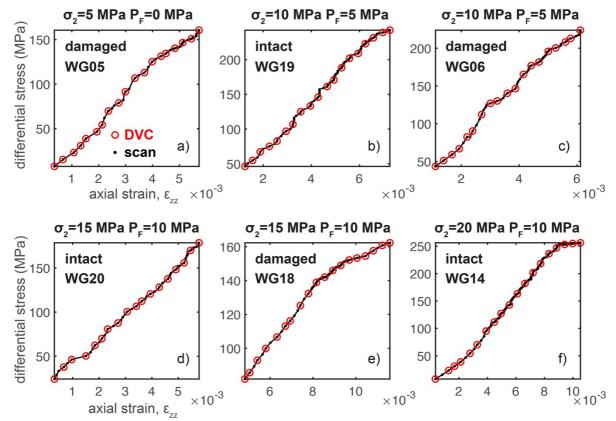


**Figure 2**. Differential stress and cumulative axial strain,  $\varepsilon_{zz}$ , when each tomogram or scan was acquired (black symbols) and the conditions of the scans used in the digital volume correlation (DVC) analyses (red symbols) for each experiment. The applied confining stress,  $\sigma_2$ , fluid pressure,  $P_F$ , and whether the core was heat-treated (damaged) before the experiment or not (intact) are listed at the top of each plot. The differential stress and  $\varepsilon_{zz}$  of the first scans shown here are not zero because we do not show the scans that were acquired during the early phase of each experiment when the axial strain-differential stress curve is highly non-linear and concave upward. This non-linearity is caused in part by the closure of preexisting fractures and pores, and to a larger extent by the settling of the rock core inside the apparatus as it comes in contact with the upper and lower pistons. We only include the scans following this non-linear stage in the digital volume correlation analysis.

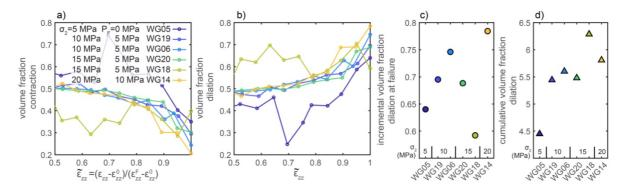
#### 3 Results

## 3.1. Evolution of the spatial localization of the strain components

To quantify the spatial localization of the contraction, |I1 < 0|, dilation, I1 > 0, and shear strain, I2, we compare the volume of the polyhedron that surrounds high values of each strain component,  $v_h$ , to the volume of the polyhedron that surrounds all of the values of the given strain component,  $v_t$ . For the shear strain,  $v_t$  is equal to the volume of the rock core used in the digital volume correlation analysis. For the volumetric strain components,  $v_t$  may be smaller than the volume of the rock core because the fraction of the rock core occupied by the dilation or contraction evolves throughout the experiment. Consequently, we first examine the evolution of this volume,  $v_t$ , divided by the volume of the total rock used in the digital volume correlation analysis for the dilation and contraction throughout each experiment. This comparison also provides insight into the influence of confining stress,  $\sigma_2$ , on volumetric strain.

183

We report the time in the experiments using the normalized cumulative macroscopic axial strain,  $\widetilde{\varepsilon_{zz}}$ . We normalize the macroscopic axial strain so that the maximum and minimum values are one and zero. In particular,  $\widetilde{\epsilon_{zz}}$  is calculated from the  $\epsilon_{zz}$  calculated for the given tomogram, the  $\varepsilon_{zz}$  of the tomogram acquired immediately preceding macroscopic failure,  $\varepsilon_{zz}^F$ , and the  $\varepsilon_{zz}$  of the first tomogram acquired at the onset of the linear phase early in loading,  $\varepsilon_{zz}^0$ , as  $\widetilde{\varepsilon_{zz}} = (\varepsilon_{zz} - \varepsilon_{zz}^0)/(\varepsilon_{zz}^F - \varepsilon_{zz}^0)$ .



189

190

191

192

193

194

199

200

201

202 203

204

205

Figure 3. Fraction of the volume of the rock occupied by contraction, I1 < 0 (a) and dilation, I1 > 0 (b) as a function of the normalized cumulative macroscopic axial strain,  $\widetilde{\varepsilon_{zz}}$ , of the second tomogram used in each digital volume correlation calculation, and the incremental (c) and sum of the incremental, or cumulative, fraction occupied by dilation (d) at the end of each experiment. The normalized cumulative macroscopic axial strain,  $\widetilde{\varepsilon_{zz}}$ , is a function of the  $\varepsilon_{zz}$  calculated from the given tomogram, the  $\varepsilon_{zz}$  of the tomogram acquired immediately preceding macroscopic failure,  $\varepsilon_{zz}^F$ , and the  $\varepsilon_{zz}$  of the first tomogram acquired at the onset of the linear phase early in loading,  $\varepsilon_{zz}^0$ , as  $\widetilde{\varepsilon_{zz}} = (\varepsilon_{zz} - \varepsilon_{zz}^0)/(\varepsilon_{zz}^F - \varepsilon_{zz}^0)$ . The colors of the symbols indicate different experiments.

The volume fraction occupied by contraction generally decreases while the fraction occupied by dilation generally increases after about 0.8  $\widetilde{\varepsilon_{zz}}$  (Figure 3). The exception to this trend is experiment WG18. This experiment hosts relatively large volume fractions of dilation, up to 0.7, early in loading, when  $\widetilde{\varepsilon_{zz}}$  is about 0.6. This experiment may have unique behavior because as this rock core was loaded into the deformation apparatus, it developed a core-spanning fracture perpendicular to the maximum compressive stress (Figure S1). Increasing axial stress during the experiment then closed the fracture.

210

211

212

213

214

215

216

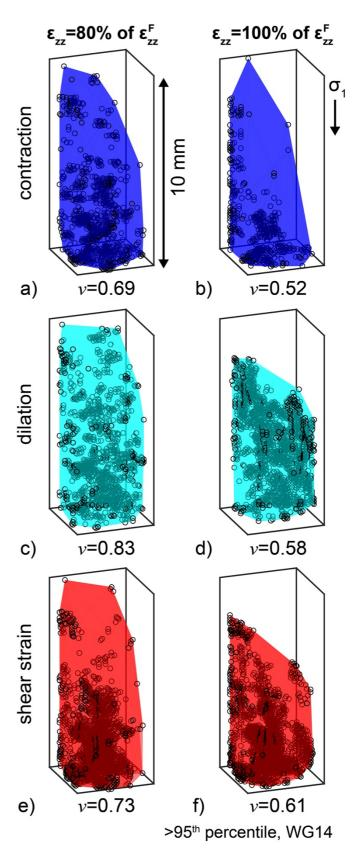
217

To assess the influence of  $\sigma_2$  on the volumetric strains, we compare the incremental volume fraction occupied by dilation immediately preceding failure, derived from the final digital volume correlation calculation, and the sum of the incremental (cumulative) volume fraction from the onset of loading to the end of the experiment. Both the incremental and cumulative strains indicate that larger  $\sigma_2$  promotes dilation (Figure 3c, d). Experiment WG14, with the largest confining stress ( $\sigma_2$ =20 MPa) and largest effective stress ( $P_e$ =10 MPa), achieves the largest incremental volume fraction occupied by dilation at the end of the experiment, and immediately preceding failure (Figure 3c), and the second largest cumulative volume fraction (Figure 3d). Experiment WG05, with the smallest  $\sigma_2$  (5 MPa), and smallest  $P_e$  (5 MPa), achieves the smallest cumulative and second smallest incremental volume fraction occupied by dilation at the end of the experiment. Experiment WG18, with  $\sigma_2$ =15 MPa and  $P_e$ =5 MPa, experiences the smallest incremental volume fraction and largest cumulative volume fraction occupied by dilation. The development of the core-spanning fracture produced a relatively high volume fraction of dilation earlier in loading in this

218 219 220

experiment compared to the other experiments. In general, greater  $\sigma_2$  and  $P_e$  promote dilation.

221 Figure 4. Spatial distribution of 222 the high values (>95<sup>th</sup> percentile) 223 of the contraction (a, b), dilation 224 (c, d) and shear strain (e, f) at  $\varepsilon_{zz}/\varepsilon_{zz}^F$ =0.80 (a, c, e), and at  $\varepsilon_{zz}/\varepsilon_{zz}^F$ =1, immediately preceding 225 226 macroscopic failure (b, d, f) for 227 experiment WG14. Black circles 228 229 show the location of the three-230 dimensional strain field with high 231 values of incremental strain, >95<sup>th</sup> 232 percentile. Shaded dark blue, light 233 blue and red areas show the 234 convex hull that fits around the 235 high strain values. The numbers 236 below each plot show the fraction 237 of the volume of the convex hull 238 relative to the total volume 239 occupied by all of the values of the strain component, v. The v of the 240 contraction, dilation, and shear 241 242 strain all decrease with increasing 243 differential stress, from 80% to 244 100% of  $\varepsilon_{zz}^F$ .



As described above, we calculate the volume of the convex hull or polyhedron that surrounds the population of the high strains,  $v_h$ , for each of the 19 digital volume correlation calculations performed in each experiment in order to quantify the spatial localization of the high strain values. We use this metric, rather than a previous metric we used to quantify the localization of strain (McBeck et al., 2022b), because this metric does not require defining a grid size, and thus the results are independent of this parameter. We report  $v_h$  divided by the volume of the polyhedron that surrounds all of the values of the given strain component,  $v_t$ , as  $v = v_h/v_t$ . Figure 4 shows the polyhedrons and resulting v found for the contractive, dilative, and shear strain values greater than the 95<sup>th</sup> percentile value at two different time steps (and digital volume correlation calculations) in experiment WG14. One of the time steps occurs immediately preceding macroscopic failure, when the  $\varepsilon_{zz}$  of the second tomogram used in the digital volume correlation analysis is equal to the  $\varepsilon_{zz}$  of the final tomogram acquired in the experiment,  $\varepsilon_{zz}^F$ , or  $\varepsilon_{zz}/\varepsilon_{zz}^F = 1$ . The other time step is earlier in the experiment, when  $\varepsilon_{zz}/\varepsilon_{zz}^F = 0.8$ . These example polyhedrons show that the v of each strain component decreases with increasing differential stress and cumulative axial strain, indicative of localization towards macroscopic failure.

**Figure 5** shows v for each strain component and all of the experiments for two of the percentile thresholds used to identify the high strain values, the  $50^{th}$  and  $90^{th}$  percentile. We perform the analyses with six different thresholds ( $50^{th}$ ,  $60^{th}$ ,  $70^{th}$ ,  $80^{th}$ ,  $90^{th}$ ,  $95^{th}$ ), and summarize those results in subsequent sections. When the dilation or contraction are greater than the  $50^{th}$  or  $90^{th}$  percentile, all but one or two experiments (WG05 and WG18) host decreases in v after about 0.8 to 0.9  $\varepsilon_{zz}$ . For the shear strain, a smaller number of the experiments host decreases in v toward failure. The decreasing v indicates that the high strain events localize. We next quantify these decreases in v approaching macroscopic failure.

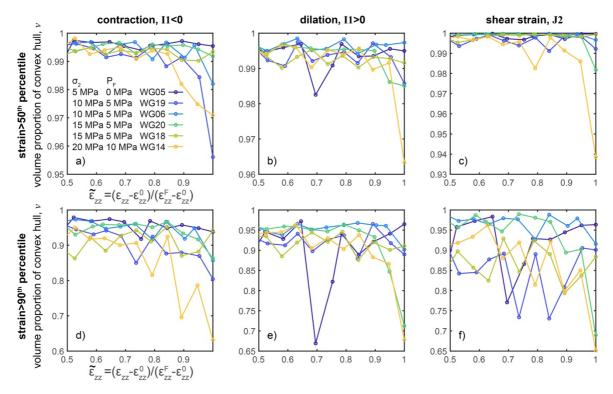


**Figure 5**. Evolution of the volume fraction of the convex hull around the high strain values, v, for strains greater than the 50<sup>th</sup> percentile (a-c) and 90<sup>th</sup> percentile (d-f), for the absolute

value of the contraction, |I1 < 0|, (a, d) dilation, I1 > 0, (b-e) and shear strain, I2 (c, f). The different colors of the curves correspond to the different experiments.

To quantify the evolution of v, we first examine the cumulative localization approaching macroscopic failure. **Figure 6** shows the absolute value of the sum of the negative values of the change in v from one digital volume correlation calculation to the next, when  $\widetilde{\varepsilon_{zz}} > 0.5$ ,  $\sum_{\widetilde{\varepsilon_{zz}} = 0.5}^{\widetilde{\varepsilon_{zz}} = 1} |\Delta v(\Delta v < 0)|$ . Negative  $\Delta v$  indicates that the volume of the polyhedron that surrounds the high strain events decreases from one digital volume correlation calculation to the next, and thus the high strain events localize from one stress step to the next. We sum the values when  $\widetilde{\varepsilon_{zz}} > 0.5$ , and not from the onset of loading, because we aim to characterize strain localization approaching macroscopic failure. Larger values of the cumulative localization thus indicate greater magnitudes of localization toward macroscopic failure.

The cumulative localization increases with the strain threshold (**Figure 6**). The analysis thus detects more localization with larger strain thresholds. This trend is expected because larger strain thresholds produce lower numbers of high strain events. The cumulative localization increases with  $\sigma_2$  for the contraction, dilation, and shear strain for all of the thresholds  $<95^{th}$  percentile (**Figure 6g-i**). When the threshold is the  $95^{th}$  percentile, the cumulative localization increases with  $\sigma_2$  for the contraction and shear strain, but not the dilation (**Figure 6h**). Dividing the experiments into groups with relatively lower and higher  $\sigma_2$  helps show that the cumulative localization increases with  $\sigma_2$  (**Figure 6d-f**). Using all of the thresholds, the mean of the cumulative localization of the contraction for the experiments with  $\sigma_2 > 10$  MPa is 36% greater than the mean of the experiments with  $\sigma_2 \le 10$  MPa. This difference is 13% and 41% for the dilation and shear strain, respectively. The generally positive slopes of the lines that fit through the cumulative localization and  $\sigma_2$  for each strain component and each threshold also indicate that larger  $\sigma_2$  produces greater cumulative localization.

The results reveal differences in the cumulative localization of the nominally intact rocks and heat-treated, damaged rocks (**Figure 6d-f**). The intact rocks tend to experience more cumulative localization than the damaged rocks. In particular, the mean of the cumulative localization of the intact rocks is 38%, 25%, and 50% greater than the mean of the damaged rocks for the contraction, dilation, and shear strain, respectively.

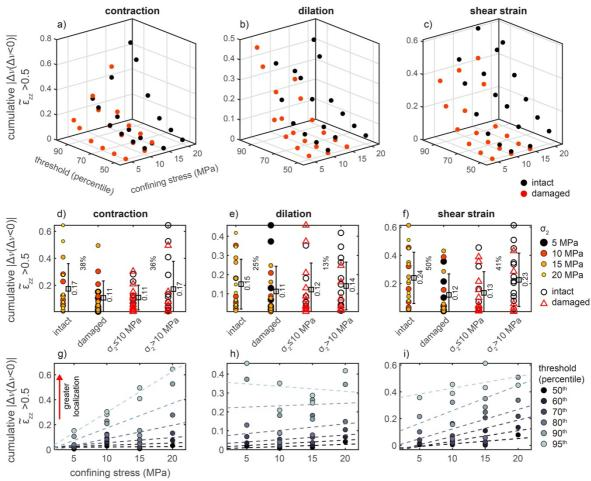


Figure 6. The cumulative localization hosted by each strain component approaching failure, calculated as the sum of the absolute value of the negative change in v when  $\widetilde{\varepsilon_{zz}} > 0.5$ ,  $\sum_{\widetilde{\varepsilon_{ZZ}}=0.5}^{\widetilde{\varepsilon_{ZZ}}=1} |\Delta v(\Delta v < 0)|$ . Negative  $\Delta v$  indicates that the volume of the polyhedron that surrounds the high strain events decreases from one digital volume correlation calculation to the next, and thus the high strain events localize from one stress step to the next. The top row (a-c) shows three-dimensional plots of the cumulative localization as a function of the applied confining stress,  $\sigma_2$ , and the thresholds used to identify the high strains for the contraction (a), dilation (b), and shear strain (c). The black and red symbols indicate if the sample was intact (black) or damaged (red). The second row (d-f) shows the cumulative localization grouped by the intact and damaged rocks, and experiments with lower  $\sigma_2$  ( $\leq 10$  MPa) and higher  $\sigma_2$  (>10 MPa). The color and size of the symbols indicate the  $\sigma_2$  for the grouping of the intact and damaged rocks. The black circles and red triangles indicate if the sample was intact (black) or damaged (red) for the grouping of the lower and higher  $\sigma_2$ . The square symbols and error bars show the mean  $\pm$  one standard deviation of each group of data points. The number next to each error bar lists the mean. The percentages between each pair of groups shows the percentage difference between the magnitude of the larger mean,  $\mu_{max}$ , and smaller mean,  $\mu_{min}$ , as  $(\mu_{max} - \mu_{min})/\mu_{max}$ . The third row (g-i) shows the cumulative localization as a function of  $\sigma_2$ . The color of the symbols indicates the threshold used to identify the high strain values. The dashed lines show the fit of the linear function through the data derived from each threshold. The intact rocks localize by larger amounts than the damaged rocks. Experiments with larger confining stress generally host more localization than experiments with lower confining stress.

304

305

306

307

308

309

310311

312

313

314

315316

317

318319

320

321

322

323

324

#### manuscript submitted to JGR Solid Earth

We also examine alternative methods of quantifying the evolution of v approaching macroscopic failure, in addition to the cumulative localization (**Figure 6**). **Figure 7** shows the localization preceding macroscopic failure measured using the difference in v from the final tomogram acquired immediately preceding failure, when  $\widetilde{\varepsilon_{zz}}$  is one, and when  $\widetilde{\varepsilon_{zz}}$  is 0.8,  $\Delta v$ . Negative  $\Delta v$  indicates that the high strain events localize towards macroscopic failure. **Figure S2** and **Figure S3** show the  $\Delta v$  calculated using  $\widetilde{\varepsilon_{zz}}$  of 0.5 and using  $\widetilde{\varepsilon_{zz}}$  of 0.9, which produce similar results to those reported for when  $\widetilde{\varepsilon_{zz}}$  is 0.8.

Using all of the tested combinations of strain components, experiments, high strain thresholds, and selected  $\widetilde{\varepsilon_{zz}}$ ,  $\Delta v$  is negative in 75% of the tested combinations. This high rate indicates that the vast majority of strain components localize toward failure. However, this rate varies among the different strain components. For the dilation and contraction,  $\Delta v$  is negative in 80% of the tested combinations. For the shear strain, in contrast,  $\Delta v$  is negative in only 67% of the tested combinations. Consequently, the volumetric strain components are more likely to experience localization approaching macroscopic failure than the shear strain.

The trends observed in this localization metric (**Figure 7**, **Figure S2**, **Figure S3**) are similar to those observed for the cumulative localization (**Figure 6**). The amount of localization increases with the high strain threshold and  $\sigma_2$ , producing increasingly negative  $\Delta v$  (**Figure 7g-i**). Consequently, the experiments with higher  $\sigma_2$  localize more than the experiments with lower  $\sigma_2$ . In addition, the intact rocks localize more than the damaged rocks. The trends observed here also occur when we calculate  $\Delta v$  using  $\widetilde{\varepsilon_{zz}}$ =0.5, and  $\widetilde{\varepsilon_{zz}}$ =0.9 (**Figure S2**, **Figure S3**), and for the v observed in the final digital volume correlation calculation, which captures the strain field immediately preceding macroscopic failure (**Figure S4**).

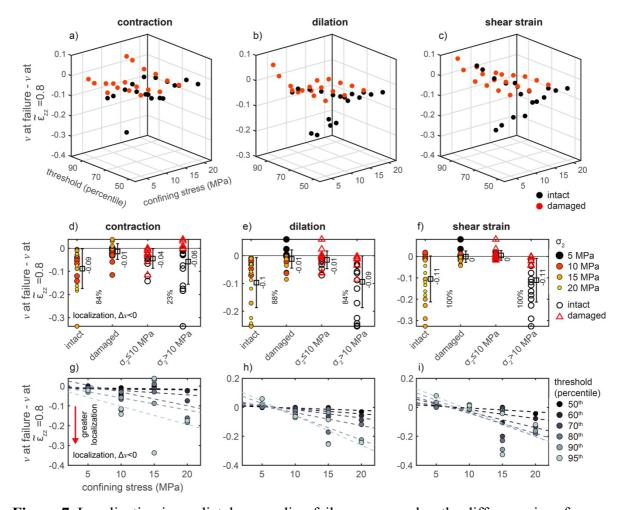


**Figure 7**. Localization immediately preceding failure measured as the difference in v from the final tomogram acquired immediately preceding failure, when  $\widetilde{\varepsilon_{zz}}$  is one, and when  $\widetilde{\varepsilon_{zz}}$  is 0.8,  $\Delta v$ . Negative  $\Delta v$  indicates that the high strain events localize towards macroscopic failure. The format of the figure is the same as **Figure 6**. The intact rocks experience larger amounts of localization preceding macroscopic failure, more negative  $\Delta v$ , than the damaged rocks. The experiments with larger confining stress host more localization than experiments with lower confining stress.

To compare the influence of  $\sigma_2$  on localization, we now report the slope of the line that fits  $\sigma_2$  and 1)  $\Delta v$  from  $\widetilde{\varepsilon_{zz}}$ =0.5, 0.8 or 0.9 to macroscopic failure, 2) the cumulative localization, and 3) v at the end of each experiment (**Figure 8**). These slopes approximate the influence of  $\sigma_2$  on localization near failure for each strain component. **Figure 6**, **Figure 7**, and **Figures S2-S4** show these lines. **Figure S5** shows the slopes derived from all the strain thresholds, and **Figure 8** shows the slopes derived using a threshold of the 90<sup>th</sup> percentile. Higher percentile thresholds produce larger slopes (**Figure S5**), and so we focus on one percentile here in order to highlight the trends observed for the other percentiles.

For each of the localization metrics except the cumulative localization, the dilation and shear strain produce larger negative slopes than the contraction (**Figure 8**). This result indicates that  $\sigma_2$  has a stronger influence on the amount of localization near failure for the dilation and shear strain than the contraction. For the cumulative localization, the slopes of the shear strain and contraction are more negative than the slope of the dilation, indicating that  $\sigma_2$  has a weaker influence on the amount of cumulative localization approaching failure

for the dilation than the shear strain or contraction. The relative magnitudes of the slopes of the cumulative localization may differ from the slopes of the other metrics because the cumulative localization of the experiment WG05, with the lowest  $\sigma_2$ , is similar to the cumulative localization of the experiments with higher  $\sigma_2$ . The large and sudden decrease in v for the dilation at  $\widetilde{\varepsilon_{zz}}$  of 0.7 produces large cumulative localization for experiment WG05 relative to the other experiments with lower  $\sigma_2$  (**Figure 5**). This temporary decrease in v, however, does not produce similarly anomalous values of  $\Delta v$  calculated using  $\widetilde{\varepsilon_{zz}}$  of 0.5, 0.8 and 0.9, or the v at macroscopic failure. Consequently, the other localization metrics are not influenced by this temporary decrease, and in general,  $\sigma_2$  has a larger influence on the dilation and shear strain than the contraction.

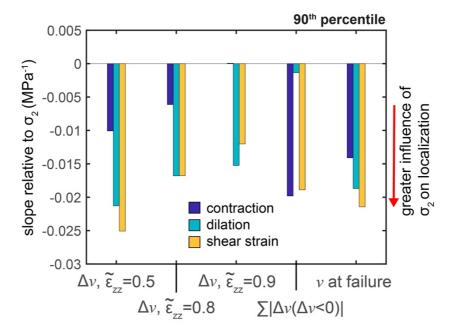


**Figure 8.** Slopes of the linear fit of different localization metrics for strains >90<sup>th</sup> percentile and  $\sigma_2$  of the experiments for each strain component: contraction (dark blue), dilation (light blue), and shear strain (yellow). The horizontal axis indicates the localization metrics: 1-3)  $\Delta v$  using  $\widetilde{\varepsilon_{zz}}$ =0.5,  $\widetilde{\varepsilon_{zz}}$ =0.8, and  $\widetilde{\varepsilon_{zz}}$ =0.9, 4) the cumulative localization, and 5) v at failure. The slopes derived from the cumulative localization were multiplied by negative one so that larger negative values indicate a stronger influence of  $\sigma_2$  on localization for all the metrics. The lines that produce each slope are shown in **Figure 6**, **Figure 7**, **Figure S2**, **Figure S3**, and **Figure S4**. In all but one of the localization metrics, the  $\sigma_2$  has a larger influence on the dilation and shear strain than the contraction.

### 3.2. Phases of delocalization and localization

The previous section focuses on the change in localization preceding macroscopic failure. Here, we compare the proportion of the experiment time, in terms of  $\widetilde{\varepsilon_{zz}}$ , that each strain component is localizing, and the timing of when the maximum localization occurs relative to macroscopic failure. In an ideal system that lacks significant heterogeneities, one may expect that the high strain values would continually localize with increasing axial strain or differential stress (Lyakhovsky et al., 2011). Consequently, the proportion of  $\widetilde{\varepsilon_{zz}}$  in which the  $\Delta v$  from one digital volume correlation calculation to the next is less than zero should be one. However, for all of the tested strain thresholds, strain components, and experiments, this proportion is always less than one, indicating that the high strains experience temporary

episodes of delocalization (**Figure 9**). The intact rocks tend to experience localization for a longer proportion of  $\widetilde{\varepsilon_{zz}}$  than the damaged rocks (**Figure 9d-f**). On average, the intact rocks experience localization for 13% (contraction), 23% (dilation), and 16% (shear strain) more  $\widetilde{\varepsilon_{zz}}$  than the damaged rocks. Thus, the damaged rocks have longer total phases of delocalization than the intact rocks.

For the dilation and shear strain, the experiments with higher  $\sigma_2$  tend to host localization for a longer period of  $\widetilde{\varepsilon_{zz}}$  than the experiments with lower  $\sigma_2$ . The experiments with  $\sigma_2 > 10$  MPa host localization on average for 24% (dilation) and 25% (shear) more  $\widetilde{\varepsilon_{zz}}$  than the experiments with  $\sigma_2 \leq 10$  MPa (**Figure 9f**). For the contraction, the experiments with  $\sigma_2 \leq 10$  MPa host slightly longer periods of  $\widetilde{\varepsilon_{zz}}$  with localization (8%) than the experiments with  $\sigma_2 > 10$  MPa.

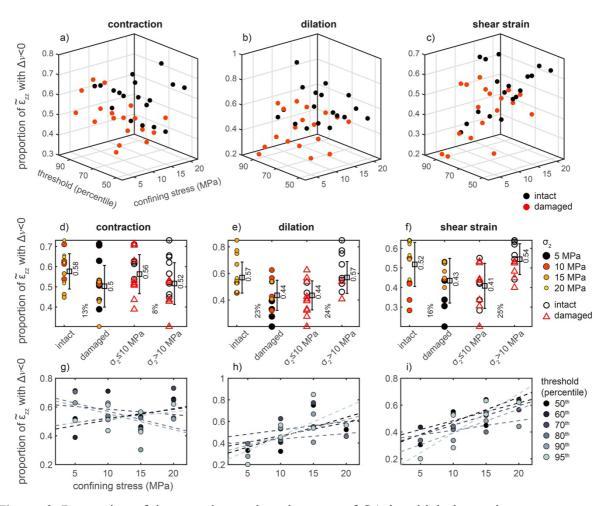
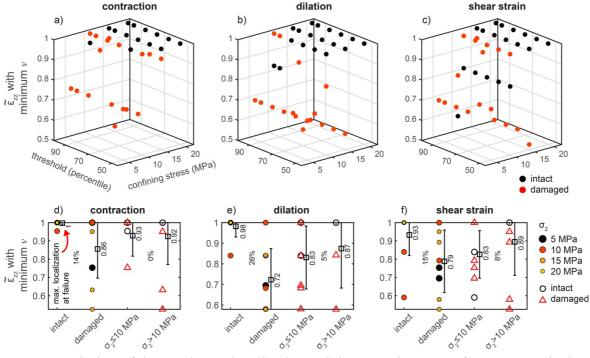


Figure 9. Proportion of the experiment time, in terms of  $\widetilde{\varepsilon}_{zz}$ , in which the strain component produces negative  $\Delta v$ , and thus localizes. Format is the same as Figure 6. The intact rocks experience larger proportions of  $\widetilde{\varepsilon}_{zz}$  in which the strain components localize than the damaged rocks. The experiments with larger confining stress generally host more  $\widetilde{\varepsilon}_{zz}$  in which the strain components localize.

These results indicate that the high strain values do not systematically increase in localization with increasing differential stress or axial strain. Instead, they experience episodes of delocalization, rather than a continuous increase or acceleration of localization toward catastrophic failure. **Figure 10** shows the  $\widetilde{\varepsilon_{zz}}$  when each strain component

experiences its minimum v, and thus maximum localization. The damaged rocks host their maximum localization earlier in loading than the intact rocks (**Figure 10d-f**). The maximum localization occurs on average at  $\widetilde{\epsilon_{zz}}$  of 0.86, 0.72, and 0.79 for the contraction, dilation and shear strain, respectively, of the damaged rocks. In contrast, for the intact rocks, the maximum localization occurs on average at  $\widetilde{\epsilon_{zz}}$  of 1, 0.98, and 0.93 for the contraction, dilation and shear strain, respectively. The differences in  $\sigma_2$  produce only small differences in the timing of the maximum localization.



**Figure 10**. Timing of the maximum localization, minimum v, in terms of  $\widetilde{\varepsilon_{zz}}$ . Format is the same as **Figure 6** (a-f). The intact rocks tend to host their maximum localization immediately preceding failure, when  $\widetilde{\varepsilon_{zz}}$  is one. In contrast, the damaged rocks host their maximum localization earlier in loading.

#### 4 Discussion

## 4.1. The influence of confining stress on volumetric strain

Tracking the volume of the rock occupied by dilation in the experiments on damaged and intact rocks, at confining stresses of 5-20 MPa, and effective stresses of 5 MPa and 10 MPa indicates that the volume of rock that experiences dilation generally increases toward failure, particularly after about  $0.8 \ \tilde{\epsilon}_{zz}$  (Figure 3). This evolution is consistent with previous digital volume correlation analyses of X-ray tomogram triaxial compression experiments (Renard et al., 2019, McBeck et al., 2019, 2020c). The observed increase of the local, incremental dilation with increasing differential stress is also consistent with previous measurements of the macroscopic, cumulative volumetric strain of Westerly granite during triaxial compression (e.g., Brace et al., 1966, Bieniawski, 1967; Brace, 1978). In triaxial compression experiments on low porosity crystalline rocks, the macroscopic volumetric strain measured from the change in shape of the sample first evolves with the differential stress approximately linearly, with increasingly contractive values, or negative in the adopted sign convention. Then, at the onset of dilatancy, C', which may be about 50-75% of the stress at failure (Brace, 1978), the volumetric strain begins to develop increasingly dilative values, and the macroscopic dilation continually increases until macroscopic failure. The progressive

increase of the macroscopic dilation observed following C' in triaxial compression experiments is consistent with the observed acceleration of the volume of rock occupied by dilation observed in the present analysis.

Comparing the fraction of the rock core that hosts dilation immediately preceding failure among the experiments indicates that increasing  $\sigma_2$  generally promotes greater dilation (Figure 3). One may expect that greater  $\sigma_2$  would suppress dilation. Indeed, triaxial compression experiments on porous rocks such as Berea sandstone and Adamswiller sandstone show that when  $\sigma_2$  increases from 5 MPa to 40 MPa, the cumulative amount of inelastic dilation, which occurs following the onset of dilatancy and until macroscopic failure, decreases (Jamison & Teufel, 1979; Wong et al., 1997). However, for low porosity crystalline rocks, the relationship between  $\sigma_2$  and the dilation follows the opposite trend observed in the sandstone (e.g., Brace & Orange, 1968; Crouch, 1970; Paterson & Wong, 2005 p. 70), and the same trend observed in the present experiments. In particular, for Westerly granite and Witwatersrand quartzite, larger  $\sigma_2$  increases the inelastic dilation within the range of 3 to 30 MPa  $\sigma_2$  for the quartzite, and 160 to 500 MPa  $\sigma_2$  for the granite (Brace & Orange, 1968; Crouch, 1970). These results highlight a fundamental difference in the accumulation of dilatancy in low porosity crystalline rocks, in which fracture propagation and opening promotes dilatancy, and porous rocks, in which pore collapse and cataclasis may inhibit dilatancy.

To compare our results to this previous work, we calculate the amount of inelastic volumetric strain (dilation) that develops between the onset of dilatancy, C' (Brace, 1978), and macroscopic failure using the change in shape of the rock core observed in the X-ray tomograms (**Figure 11a, b**). We then compare these values to the sum of the volume fraction occupied by dilation, and the sum of the mean dilation from the onset of loading until failure calculated from the local incremental strains derived via digital volume correlation (**Figure 11c, d**). The identified values of C' are estimates based on the reversal in the slopes of the volumetric strain and differential stress curves. These estimates occur near 75% of the differential stress at failure, consistent with previous observations of the stress at C' (Brace, 1978).

Examining the macroscopic inelastic volumetric strain indicates that increasing  $\sigma_2$  generally promotes more inelastic dilation (**Figure 11b**). The two damaged experiments, WG06 and WG18, deviate from the overall trend of increasing inelastic dilation with increasing  $\sigma_2$ . These experiments produce more inelastic strain than expected from the intact experiments with the corresponding  $\sigma_2$ . Previous work shows that more preexisting damage generally produces longer macroscopic yielding phases in which more volumetric and axial strain accumulate. In particular, sandstone with some significant porosity accumulates more volumetric and axial strain than granite during triaxial compression (e.g., Feng et al., 2019). Examining the cumulative volume fraction of dilation also shows that the damaged experiments WG06 and WG18 host larger volume fractions of dilation than expected from the corresponding intact experiments (**Figure 11c**). In summary, the cumulative volume fraction (**Figure 11c**), the cumulative mean dilation (**Figure 11d**), and the macroscopic inelastic volumetric strain (**Figure 11b**) all suggest that larger  $\sigma_2$  promotes more dilation, consistent with previous measurements of low porosity crystalline rock (e.g., Brace & Orange, 1968; Crouch, 1970).

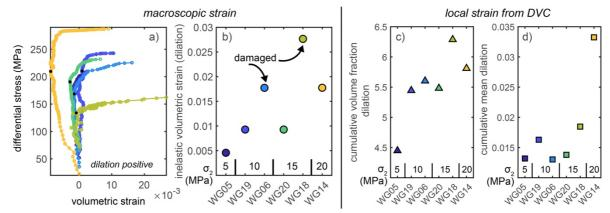


**Figure 11**. The influence of  $\sigma_2$  on dilatancy. Evolution of the volumetric strain calculated from the shape change of the rock core observed in the X-ray tomograms (a), the amount of inelastic volumetric strain between the onset of dilatancy, C', and macroscopic failure (b), and the cumulative volume fraction of the dilation (c) and cumulative mean dilation (d) calculated from the local strain derived from digital volume correlation. The black dots in (a) shows the location of C'. Increasing  $\sigma_2$  produces more dilation.

496 497

498

499

500

501

502

503

504

505

506

507

508

509

510

511

512

513

514

515516

517

518

519

520

521

522

523524

525526

527

528

529

530

## 4.2. The influence of confining stress on localization approaching macroscopic failure

Tracking the volume of the polyhedron that surrounds the high contraction, dilation and shear strain indicates that the high strain events localize approaching macroscopic failure in all three components for the vast majority of the experiments (Figure 5). However, for all the tested parameters, the dilation localizes approaching failure more often (80% of the combinations of parameters produce negative changes in volume) than the shear strain (67%) (e.g., Figure 6, Figure 7). This result is consistent with a previous analysis of the localization of the volumetric and shear strain in a different set of X-ray tomography experiments on Westerly granite, Fontainebleau sandstone, Mt. Etna basalt, Green River shale, and Anstrude limestone (McBeck et al., 2022b). In this previous analysis and the present analysis, the high magnitudes of the volumetric strains localize to a greater extent than the shear strain. In addition, in the present analysis, the maximum strain localization occurs immediately preceding failure for the dilation, on average at 0.98  $\widetilde{\epsilon_{zz}}$  for the intact rocks, but occurs earlier in loading for the shear strain, on average at 0.93  $\widetilde{\varepsilon_{zz}}$  for the intact rocks (**Figure 10**). Thus, the dilation hosts more systematic increases in localization towards failure than the shear strain, and the timing of maximum localization occurs almost exactly at macroscopic failure. Consequently, both the previous and present analyses suggest that the high magnitudes of the volumetric strains may provide more reliable information about the timing of catastrophic failure than the shear strain. Indeed, machine learning analyses indicate that the evolution of the dilative strain helps predict the timing of macroscopic failure in X-ray tomography experiments, and that the shear strain provides less useful information about the timing of failure (McBeck et al., 2020a). However, machine learning analyses of three-dimensional discrete element method numerical models of segmented fault networks within shear zones indicate that the shear strain provides more useful information about the timing of fault reactivation and macroscopic failure than the volumetric strain (McBeck et al., 2022a). Consequently, the utility of the volumetric strains for predicting the timing of failure may depend on the tectonic environment, and the existence of system-spanning, macroscopic faults.

Comparing the degree of localization near failure among the different experiments indicates that higher  $\sigma_2$  promotes greater localization approaching macroscopic failure

(Figure 5, Figure 6, Figure 7, Figures S2-S5). In the brittle portion of the crust, strike-slip faults tend to develop flower structures: a diffuse network of fractures near the surface that then localizes into a narrower zone at depth (Harding, 1985; Sylvester, 1988; Le Guerroue & Cobbold, 2006, Rockwell & Ben-Zion, 2007) (Figure 12a). This structure implies that increasing confining stress promotes localization. In addition, seismic observations indicate that low velocity zones surrounding large crustal faults, such as the San Jacinto fault (Wang et al., 2019), can narrow with depth. Moreover, low magnitude seismicity between large magnitude earthquakes in southern and Baja California increases in localization with increasing depth (Ben-Zion & Zaliapin, 2019). Such fault zones are the result of the accumulation of many cycles of fault growth, including coseismic slip and precursory localization. Here, we show that in one cycle of precursory deformation leading to macroscopic failure, greater confining stress leads to greater localization of the high strain events.

Observations of post-mortem fracture networks that form in uniaxial and triaxial compression experiments support the idea that increasing confining stress promotes localization (e.g., Paterson, 1958; Paterson & Wong, 2005 p. 212). Under uniaxial compression and low confining stresses in triaxial compression, rock cores fail by axial splitting, in which arrays of fractures aligned parallel to the maximum compression direction develop (e.g., **Figure 12b**). These fracture networks are often diffusely distributed, with several fractures extending from the top to the bottom of the core (e.g., Akdag et al., 2021; Basu et al. 2013; Hu et al., 2021). Under higher confining stresses, the rock cores fail through the development of one or a few macroscopic shear fractures, perhaps as a pair as conjugate shear fractures (e.g., Paterson, 1958; Lee & Rathnaweera, 2016). Although these fractures may develop from the coalescence of many small fractures, the final fracture geometry identified following the maximum stress consists of a few system-spanning fractures. Consequently, the fracture geometries that develop under uniaxial compression and low confining stress tend to be less localized than the fracture geometries that develop at higher confining stresses.

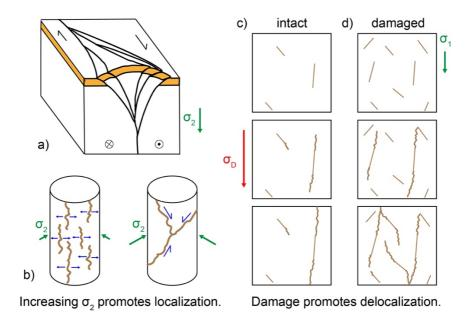


**Figure 12.** Examples of increasing confining stress promoting localization (a-b), and preexisting damage promoting delocalization (c-d). a) Positive flower structures that develop along strike-slip fault networks host a diffuse network of fractures at the surface that localize

into a narrower zone with depth. b) The tensile-dominated fracture networks that develop under low confining stress or uniaxial compression tend to be more diffusely spread (left) than the shear-dominated fracture networks that coalesce under higher confining stress (right). c) With lower amounts of preexisting damage, only a few of the longest and most favorably oriented fractures grow under increasing differential stress. d) With more preexisting damage, several of the smaller fractures may grow, rather than the few longest fractures, thereby producing delocalization.

 A network of fractures dominated by shear may be more localized than a network dominated by tension because the stress concentrations that develop at preexisting fractures and heterogeneities may be more important for the coalescence of shear fractures than the propagation of extensile fractures. Because the tensile strength of rocks is lower than the shear strength (Paterson & Wong, 2005 p. 22), extensile fractures may more easily develop throughout the rock core than shear fractures. Shear fractures may thus depend on the stress concentrations that develop near preexisting fractures in order to propagate and coalesce to a greater extent than the extensile fractures. Consequently, the shear fractures may be more likely to develop near preexisting fractures than the extensile fractures, producing more localized fault networks. Consistent with these theoretical arguments, laboratory observations, and crustal observations of fault structures at depth, the present analysis shows that increasing confining stress promotes greater increases in localization of the high strain events approaching macroscopic failure.

# 4.3. The influence of preexisting damage on localization approaching macroscopic failure

The present analysis shows that rocks can experience temporary episodes of delocalization, rather than a continuous increase or acceleration of localization toward catastrophic failure (e.g., **Figure 5**). This result is consistent with previous analyses of fracture development (McBeck et al., 2021a) and strain localization (McBeck et al., 2022b) in X-ray tomography triaxial compression experiments. This previous analysis found that the maximum strain localization generally occurs near 90% of the differential stress at macroscopic failure, rather than at macroscopic failure (McBeck et al., 2022b). In particular, only 46% of the experiments achieve maximum localization at macroscopic failure, or >99% of the failure stress. These results are similar to the damaged rocks in present analysis. For the damaged rocks, the maximum strain localization occurs on average at 94% (contraction), 86% (dilation), and 90% (shear strain) of the differential stress at failure. In contrast, for the intact rocks, the maximum strain localization occurs immediately preceding failure, and on average at 99% (contraction and dilation), and 95% (shear strain) of the differential stress at failure (**Figure 10**).

The results of the previous analysis (McBeck et al., 2022b) may be more consistent with the results of the damaged Westerly granite than the intact Westerly granite because the majority of the experiments used in the previous analysis were performed on rocks with more preexisting pores and fractures than the intact Westerly granite, such as Fontainebleau sandstone and Mt. Etna basalt. The localization behavior of sandstone and basalt is expected to be more similar to damaged Westerly granite than intact Westerly granite because the presence of preexisting damage can influence fracture development (e.g., Helgeson & Aydin, 1991; Tang et al., 2000; d'Alession & Martel, 2004; Gudmundsson et al., 2010; Cartwright-Taylor et al., 2020; Vasseur et al., 2015), and deformation localization (McBeck et al. 2021b). For example, analyses of fracture development in numerical models show that more heterogeneous models produce more precursors than less heterogeneous models (Tang et al., 2000). The precursors in the more heterogeneous models develop in a diffuse distribution

early in loading, and then coalesce into a system-spanning fracture that ultimately causes macroscopic failure. In contrast, in less heterogeneous models, only a few precursors develop at random positions throughout the rock, and these positions do not help indicate the final geometry of the system-spanning fracture that causes macroscopic failure. These numerical results are consistent with observations of fracture network development in X-ray tomography triaxial compression experiments on nominally intact and heat-treated (damaged) Ailsa Craig microgranite (Cartwright-Taylor et al., 2020). These experiments show that the heat-treated, and thus more heterogeneous, rock develops more precursory fractures throughout loading toward failure, producing a smooth, continuous evolution, indicative of a second-order transition (Cartwright-Taylor et al., 2020). In contrast, the nominally intact rock hosts few detectable precursors preceding macroscopic failure, producing an abrupt, or firstorder, transition. Similarly, numerical models of strike-slip faults embedded in host rock with varying amounts of preexisting weaknesses show that the fracture networks in more homogeneous models continually increase in localization toward macroscopic failure (McBeck et al., 2021b). In contrast, more heterogeneous models experience phases of delocalization superposed on the overall trend of increasing localization. Observations of low-magnitude seismicity preceding several M>7 earthquakes in Southern and Baja California reveal similar phases of delocalization (Ben-Zion & Zaliapin, 2020).

Consistent with the observed influence of heterogeneities on fracture development and localization, the present analysis shows that the damaged Westerly granite experiences maximum localization earlier in loading than the intact Westerly granite (**Figure 10**). Moreover, the proportion of the macroscopic axial strain in which the intact rocks experience localization is larger than the proportion in which the damaged rocks experience localization (**Figure 9**). In addition, the intact rocks tend to experience more cumulative localization throughout loading (**Figure 6**), greater increases in localization immediately preceding failure (**Figure 7**), and smaller v and thus greater absolute localization at failure (**Figure S4**) than the damaged rocks. Thus, more preexisting damage favors delocalization.

The damaged rocks, and more heterogeneous systems in general, may promote episodes of delocalization because the stress concentrations that develop at heterogeneities may allow fracture propagation to require less energy in a network with many smaller fractures than in a more sparsely populated fracture network with several large fractures and only a few smaller fractures (e.g., **Figure 11c**). This effect produces the decreasing strength of rocks at increasing length-scales (e.g., Lockner, 1995; Paterson & Wong, 2005 p. 31). Because larger rock volumes are more likely to contain longer fractures than smaller rock volumes, these longer fractures develop stress concentrations that trigger fracture propagation, and ultimately produce macroscopic failure at a lower level of stress than smaller rock volumes. Consequently, the existence of a diffuse network of heterogeneities enables propagation from many smaller fractures that may delocalize the overall deformation away from the few largest fractures. A diffuse fracture network would also provide a greater opportunity for stress shadows to inhibit growth between fractures (e.g., Nur, 1982) than a more clustered network, and thereby promote delocalization.

### 5 Conclusions

To assess the influence of confining stress and preexisting damage on strain localization, we perform a series of X-ray tomography triaxial compression experiments on Westerly granite, and then use digital volume correlation to estimate the local three-dimensional strain tensors throughout loading until macroscopic failure. We examine the evolving volume of the polyhedron that surrounds the highest values of three strain

657 components: the contraction, dilation, and shear strain. We find that experiments with higher confining stress (>10 MPa) host larger amounts of dilation than experiments with lower 658 confining stress, consistent with previous laboratory analyses on low porosity crystalline rock 659 660 (e.g., Brace & Orange, 1968; Crouch, 1970). Higher confining stress is also associated with larger increases in localization of the high strain events approaching macroscopic failure. 661 This positive correlation between confining stress and localization is consistent with the 662 663 localized geometry of the shear-dominated fractures that develop at higher confining stresses 664 compared to the more diffuse arrangement of the extensile-dominated fractures that develop in uniaxial compression (e.g., Paterson, 1958), and with crustal observations of strike-slip 665 666 fault networks that narrow with depth (e.g., Sylvester, 1988; Rockwell & Ben-Zion, 2007). Tracking the volume of the high strains shows that the strain events do not always 667 systematically increase in localization towards failure, but instead experience phases of 668 delocalization. This result is consistent with previous X-ray tomography triaxial compression 669 experiments (McBeck et al., 2021a; McBeck et al., 2022b), and with observations of low 670 magnitude seismicity in Southern and Baja California (Ben-Zion & Zaliapin, 2020). The 671 672 amount of preexisting damage controls the extent of the phases of delocalization, and when the rock experiences the greatest localization of the high strain events. The damaged rocks 673 674 experience longer proportions of the experiment time, in terms of the macroscopic axial 675 strain, in which the strains are delocalizing than the intact rocks. The heat-treated, and thus 676 damaged, Westerly granite experiments host the greatest localization of the high strain events 677 on average near 90% of the differential stress at failure, consistent with strain localization in 678 rocks with some preexisting porosity and heterogeneities, such as Mt. Etna basalt and Fontainebleau sandstone (McBeck et al., 2022b). In contrast, the intact Westerly granite 679 680 experiments host the greatest localization of the high strain events on average near 99% of the differential stress at failure. In addition, the high strain events localize by larger 681 682 magnitudes preceding failure in the intact rocks than the damaged rocks. Consequently, more preexisting damage favors delocalization. More preexisting damage may allow more 683 684 delocalization because the stress concentrations that develop at preexisting heterogeneities 685 periodically enable smaller fractures to propagate, and form stress shadows that inhibit growth. The results show that the dilation hosts more systematic increases in localization 686 687 towards failure than the shear strain, consistent with a previous digital volume correlation 688 analysis (McBeck et al., 2022b), and that the timing of maximum localization occurs almost exactly at macroscopic failure, consistent with a machine learning analysis that found that the 689 690 dilative strain helps predict the timing of catastrophic failure better than the shear strain 691 (McBeck et al., 2020a). Consequently, the dilative strain may provide more reliable 692 information about the timing of catastrophic failure than the shear strain.

# Acknowledgements

693

700

- The Research Council of Norway (grant 300435 to JM), U.S. National Science Foundation
- 695 (grant EAR-2122168 to YBZ) and the European Research Council under the European
- Union's Horizon 2020 research and innovation program (grant No. 101019628 BREAK to
- 697 FR) funded this work. Beamtime was allocated at the European Synchrotron Radiation
- 698 Facility (Long Term Proposal ES-1190). We thank Clémence Muzelle for technical support
- on beamline ID19 at ESRF.

# Open Research

- 701 The experimental data (time series of X-ray tomograms) are available on Norstore with DOI
- 702 10.11582/2023.00007
- 703 (https://archive.norstore.no/pages/public/datasetDetail.jsf?id=10.11582/2023.00007).

### 704 References

- Akdag, S., Karakus, M., Nguyen, G. D., Taheri, A., & Bruning, T. (2021). Evaluation of the
- propensity of strain burst in brittle granite based on post-peak energy analysis. Underground
- 707 Space, 6(1), 1-11.
- 708 Basu, A., Mishra, D. A., & Roychowdhury, K. (2013). Rock failure modes under uniaxial
- 709 compression, Brazilian, and point load tests. Bulletin of Engineering Geology and the
- 710 Environment, 72, 457-475.
- 711 Ben-Zion, Y. and I. Zaliapin, (2019). Spatial variations of rock damage production by
- earthquakes in southern California, Earth and Planetary Science Letters, 512, 184–193.
- 713 Ben-Zion, Y., & Zaliapin, I. (2020). Localization and coalescence of seismicity before large
- earthquakes. Geophysical Journal International, 223(1), 561-583.
- 715 Benson, P. M., Thompson, B. D., Meredith, P. G., Vinciguerra, S., & Young, R. P. (2007).
- 716 Imaging slow failure in triaxially deformed Etna basalt using 3D acoustic-emission location
- and X-ray computed tomography. Geophysical Research Letters, 34(3), L03303.
- 718 Bieniawski, Z. T. (1967). Mechanism of brittle fracture of rock: Part I. Theory of the fracture
- 719 process. Part II. Experimental studies; Part III. Fracture in tension and under long-term
- 720 loading. International Journal of Rock Mechanics and Mining Sciences & Geomechanics
- 721 Abstracts, 4(4), 395-406.
- 722 Brace, W. F. (1978). Volume changes during fracture and frictional sliding: A review. Pure
- 723 and Applied Geophysics, 116, 603-614.
- Prace, W. F., & Orange, A. S. (1968). Electrical resistivity changes in saturated rocks during
- fracture and frictional sliding. Journal of Geophysical Research, 73(4), 1433-1445.
- 726 Brace, W. F., Paulding Jr, B. W., & Scholz, C. H. (1966). Dilatancy in the fracture of
- 727 crystalline rocks. Journal of Geophysical Research, 71(16), 3939-3953.
- Buades, A., Coll, B., & Morel, J. M. (2005). A non-local algorithm for image denoising. In
- 729 2005 IEEE Computer Society Conference on Computer Vision and Pattern Recognition
- 730 (CVPR'05), 2, 60-65.
- 731 Cartwright-Taylor, A., Main, I. G., Butler, I. B., Fusseis, F., Flynn, M., & King, A. (2020).
- 732 Catastrophic failure: how and when? Insights from 4-D in situ x-ray microtomography.
- Journal of Geophysical Research: Solid Earth, 125(8), e2020JB019642.
- Charalampidou, E. M., Hall, S. A., Stanchits, S., Lewis, H., & Viggiani, G. (2011).
- 735 Characterization of shear and compaction bands in a porous sandstone deformed under
- 736 triaxial compression. Tectonophysics, 503(1-2), 8-17.
- 737 Crouch, S. L. (1970). Experimental determination of volumetric strains in failed rock. In
- 738 International Journal of Rock Mechanics and Mining Sciences & Geomechanics Abstracts,
- 739 7(6), 589-603.
- 740 d'Alessio, M. A., & Martel, S. J. (2004). Fault terminations and barriers to fault growth.
- 741 Journal of Structural Geology, 26(10), 1885-1896.
- Feng, X. T., Kong, R., Zhang, X., & Yang, C. (2019). Experimental study of failure
- 743 differences in hard rock under true triaxial compression. Rock Mechanics and Rock
- 744 Engineering, 52, 2109-2122.
- 745 Fredrich, J. T., & Wong, T. F. (1986). Micromechanics of thermally induced cracking in
- three crustal rocks. Journal of Geophysical Research: Solid Earth, 91(B12), 12743-12764.

- Griffiths, L., Heap, M. J., Baud, P., & Schmittbuhl, J. (2017). Quantification of microcrack
- characteristics and implications for stiffness and strength of granite. International Journal of
- Rock Mechanics and Mining Sciences, 100, 138-150.
- Gudmundsson, A., Simmenes, T. H., Larsen, B., & Philipp, S. L. (2010). Effects of internal
- structure and local stresses on fracture propagation, deflection, and arrest in fault zones.
- 752 Journal of Structural Geology, 32(11), 1643-1655.
- Gueydan, F., Précigout, J., & Montesi, L. G. (2014). Strain weakening enables continental
- 754 plate tectonics. Tectonophysics, 631, 189-196.
- Harding, T. P. (1985). Seismic characteristics and identification of negative flower structures,
- positive flower structures, and positive structural inversion. AAPG bulletin, 69(4), 582-600.
- 757 Helgeson, D. E., & Aydin, A. (1991). Characteristics of joint propagation across layer
- interfaces in sedimentary rocks. Journal of Structural Geology, 13(8), 897-911.
- 759 Hu, J., Zeng, P., Yang, D., Wen, G., Xu, X., Ma, S., Zhao, F., & Xiang, R. (2021).
- 760 Experimental investigation on uniaxial compression mechanical behavior and damage
- evolution of pre-damaged granite after cyclic loading. Energies, 14(19), 6179.
- Jamison, W. R., & Teufel, L. W. (1979). Pore volume changes associated with failure and
- 763 frictional sliding of a porous sandstone. 20th US Symposium on Rock Mechanics (USRMS).
- 764 OnePetro.
- Le Guerroué, E., & Cobbold, P. R. (2006). Influence of erosion and sedimentation on strike-
- slip fault systems: insights from analogue models. Journal of Structural Geology, 28(3), 421-
- 767 430.
- Lee, B., & Rathnaweera, T. D. (2016). Stress threshold identification of progressive
- 769 fracturing in Bukit Timah granite under uniaxial and triaxial stress conditions. Geomechanics
- and Geophysics for Geo-Energy and Geo-Resources, 2, 301-330.
- 771 Lockner, D. A. (1995). Rock failure: Rock Physics and Phase Relations. A Handbook of
- Physical Constants. Am. Geophys. Union Reference Shelf. Am. Geophys. Union, 127-141.
- Lockner, D., Byerlee, J. D., Kuksenko, V., Ponomarev, A., & Sidorin, A. (1991). Quasi-static
- fault growth and shear fracture energy in granite. Nature, 350(6313), 39-42.
- 775 Lyakhovsky, V., Hamiel, Y., & Ben-Zion, Y. (2011). A non-local visco-elastic damage
- model and dynamic fracturing. Journal of the Mechanics and Physics of Solids, 59(9), 1752-
- 777 1776.
- McBeck, J., Aiken, J. M., Ben-Zion, Y., & Renard, F. (2020a). Predicting the proximity to
- 779 macroscopic failure using local strain populations from dynamic in situ X-ray tomography
- triaxial compression experiments on rocks. Earth and Planetary Science Letters, 543, 116344.
- 781 McBeck, J. A., Aiken, J. M., Mathiesen, J., Ben-Zion, Y., & Renard, F. (2020b). Deformation
- 782 precursors to catastrophic failure in rocks. Geophysical Research Letters, 47(24),
- 783 e2020GL090255.
- McBeck, J., Ben-Zion, Y., & Renard, F. (2020c). The mixology of precursory strain
- partitioning approaching brittle failure in rocks. Geophysical Journal International, 221(3),
- 786 1856-1872.
- 787 McBeck, J., Ben-Zion, Y., & Renard, F. (2021a). Fracture network localization preceding
- catastrophic failure in triaxial compression experiments on rocks. Frontiers in Earth Science,
- 789 9, 778811.

- 790 McBeck, J., Ben-Zion, Y., & Renard, F. (2022a). Predicting fault reactivation and
- 791 macroscopic failure in discrete element method simulations of restraining and releasing step
- 792 overs. Earth and Planetary Science Letters, 593, 117667.
- 793 McBeck, J., Ben-Zion, Y., & Renard, F. (2022b). Volumetric and shear strain localization
- throughout triaxial compression experiments on rocks. Tectonophysics, 822, 229181.
- McBeck, J., Ben-Zion, Y., Zhou, X., & Renard, F. (2021b). The influence of preexisting host
- rock damage on fault network localization. Journal of Structural Geology, 153, 104471.
- 797 McBeck, J. A., Cordonnier, B., Vinciguerra, S., & Renard, F. (2019). Volumetric and shear
- strain localization in Mt. Etna basalt. Geophysical Research Letters, 46(5), 2425-2433.
- 799 McBeck, J., Kobchenko, M., Hall, S. A., Tudisco, E., Cordonnier, B., Meakin, P., & Renard,
- 800 F. (2018). Investigating the onset of strain localization within anisotropic shale using digital
- volume correlation of time-resolved X-ray microtomography images. Journal of Geophysical
- 802 Research: Solid Earth, 123(9), 7509-7528.
- 803 Mulyukova, E., & Bercovici, D. (2019). The generation of plate tectonics from grains to
- global scales: A brief review. Tectonics, 38(12), 4058-4076.
- Nur, A. (1982). The origin of tensile fracture lineaments. Journal of Structural Geology, 4(1),
- 806 31-40.
- Paterson, M. S. (1958). Experimental deformation and faulting in Wombeyan marble.
- 808 Geological Society of America Bulletin, 69(4), 465-476.
- Paterson, M. S., & Wong, T. F. (2005). Experimental rock deformation: the brittle field, 348.
- 810 Berlin: Springer.
- Renard, F., Cordonnier, B., Dysthe, D. K., Boller, E., Tafforeau, P., & Rack, A. (2016). A
- deformation rig for synchrotron microtomography studies of geomaterials under conditions
- down to 10 km depth in the Earth. Journal of Synchrotron Radiation, 23(4), 1030-1034.
- Renard, F., McBeck, J., Kandula, N., Cordonnier, B., Meakin, P., & Ben-Zion, Y. (2019).
- Volumetric and shear processes in crystalline rock approaching faulting. Proceedings of the
- 816 National Academy of Sciences, 116(33), 16234-16239.
- 817 Rockwell, T. K., & Ben-Zion, Y. (2007). High localization of primary slip zones in large
- 818 earthquakes from paleoseismic trenches: Observations and implications for earthquake
- physics. Journal of Geophysical Research: Solid Earth, 112(B10).
- Rudnicki, J. W., & Rice, J. R. (1975). Conditions for the localization of deformation in
- pressure-sensitive dilatant materials. Journal of the Mechanics and Physics of Solids, 23(6),
- 822 371-394.
- 823 Satoh, T., Shivakumar, K., Nishizawa, O., & Kusunose, K. (1996). Precursory localization
- and development of microfractures along the ultimate fracture plane in amphibolite under
- triaxial creep. Geophysical Research Letters, 23(8), 865-868.
- 826 Sylvester, A. G. (1988). Strike-slip faults. Geological Society of America Bulletin, 100(11),
- 827 1666-1703.
- 828 Tang, C. A., Liu, H., Lee, P. K. K., Tsui, Y., & Tham, L. (2000). Numerical studies of the
- influence of microstructure on rock failure in uniaxial compression—part I: effect of
- heterogeneity. International Journal of Rock Mechanics and Mining Sciences, 37(4), 555-
- 831 569.

### manuscript submitted to JGR Solid Earth

- 832 Tudisco, E., Andò, E., Cailletaud, R., & Hall, S. A. (2017). TomoWarp2: A local digital
- volume correlation code. SoftwareX, 6, 267-270.
- Vasseur, J., Wadsworth, F. B., Lavallée, Y., Bell, A. F., Main, I. G., & Dingwell, D. B.
- 835 (2015). Heterogeneity: The key to failure forecasting. Scientific Reports, 5(1), 13259.
- Wang, Y., Allam, A., & Lin, F. C. (2019). Imaging the fault damage zone of the San Jacinto
- fault near Anza with ambient noise tomography using a dense nodal array. Geophysical
- 838 Research Letters, 46(22), 12938-12948.
- Wong, T. F., David, C., & Zhu, W. (1997). The transition from brittle faulting to cataclastic
- 840 flow in porous sandstones: Mechanical deformation. Journal of Geophysical Research: Solid
- 841 Earth, 102(B2), 3009-3025.

Figure 1.	
-----------	--

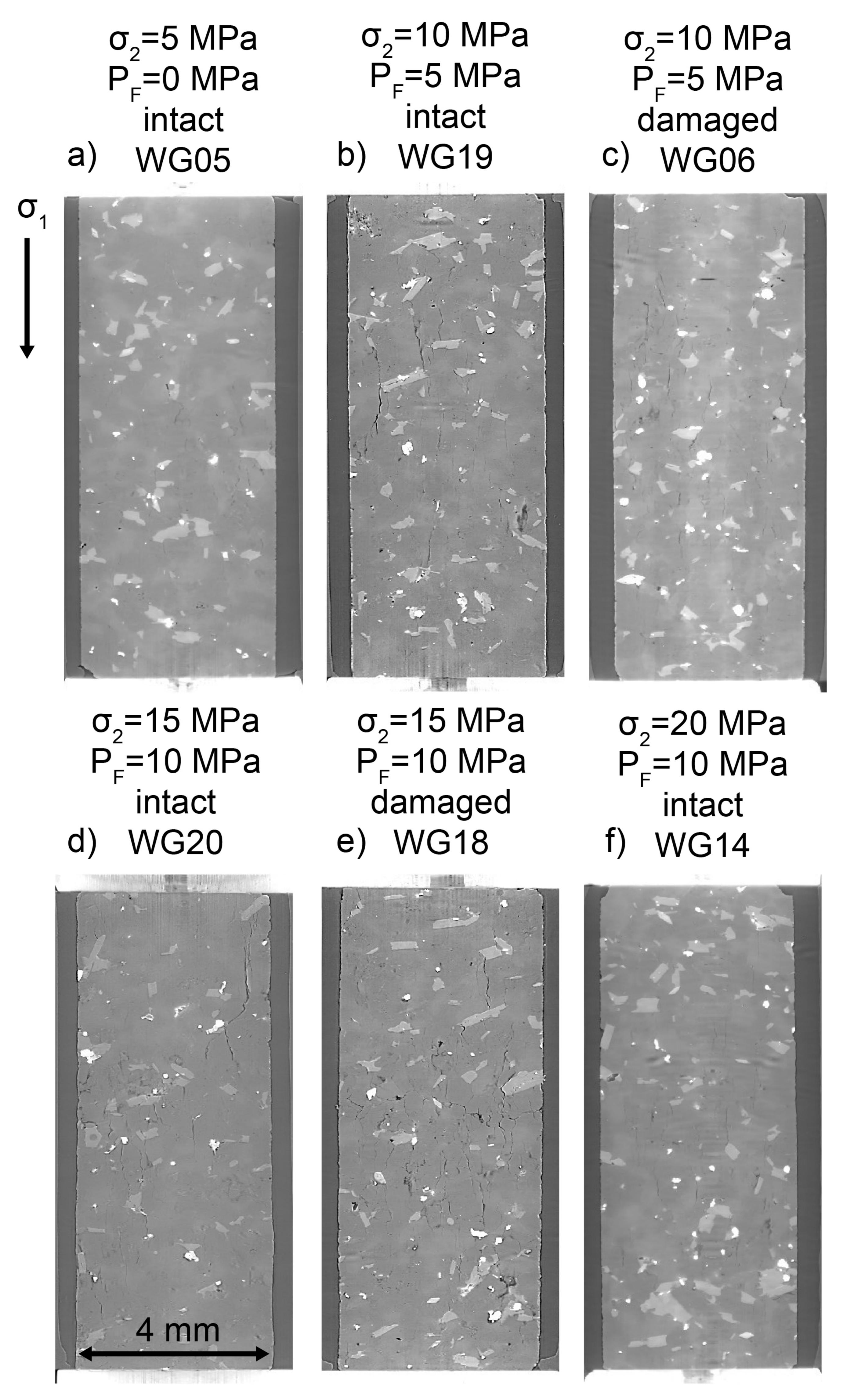


Figure 2	2.
----------	----

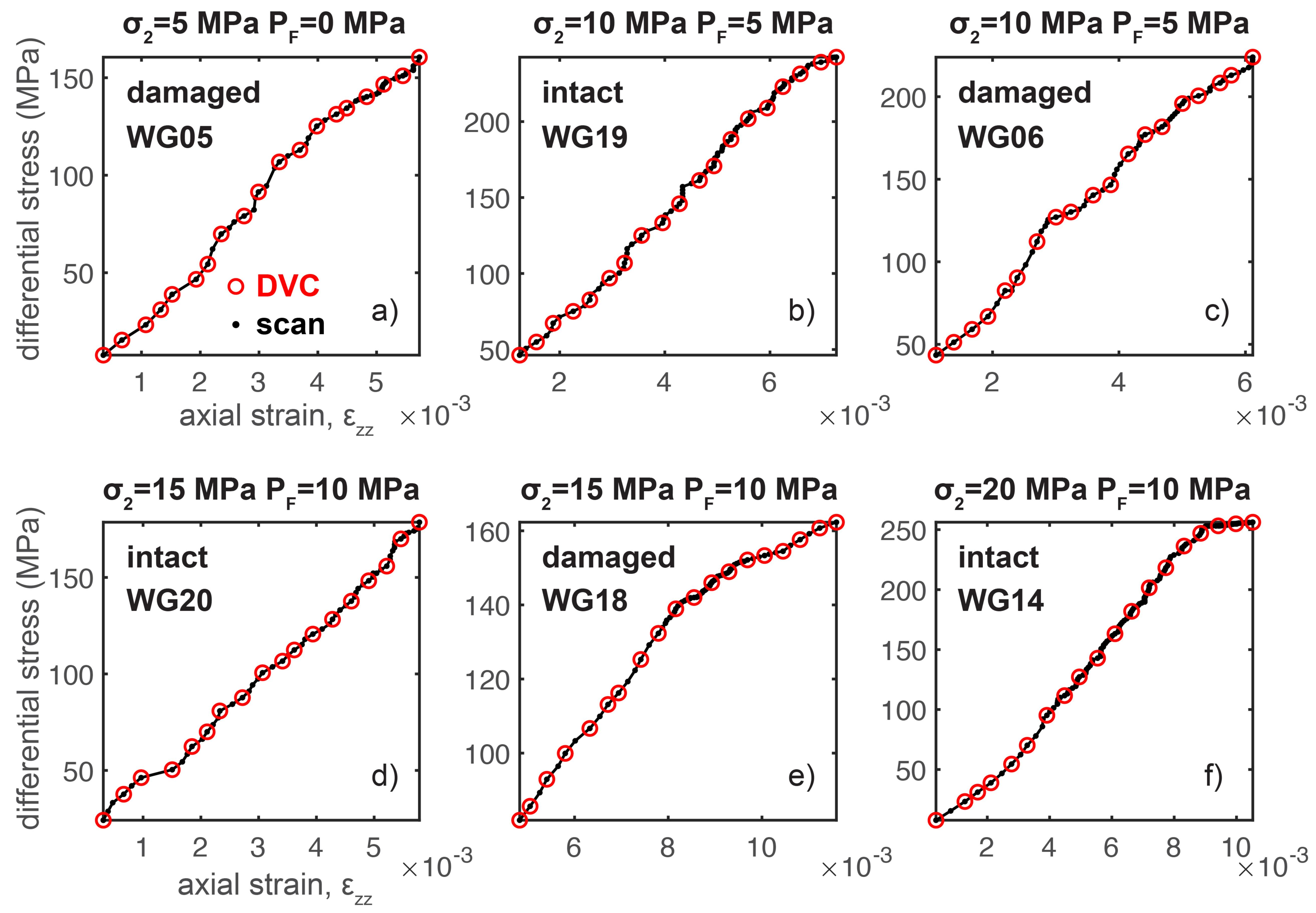


Figure	3.
--------	----

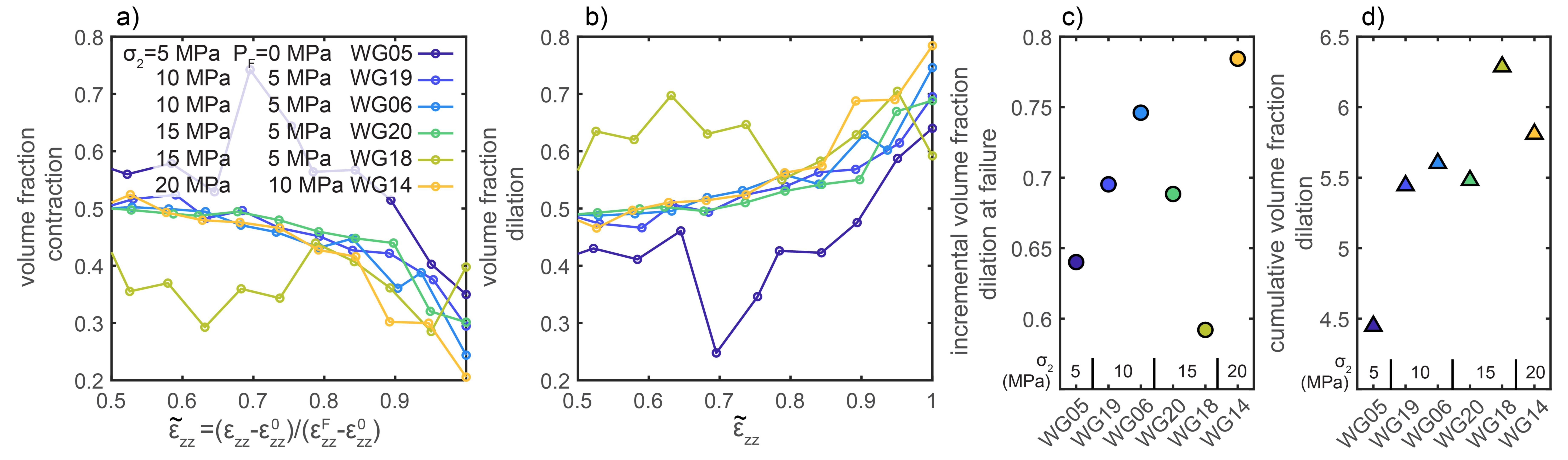


Figure 4.	
-----------	--

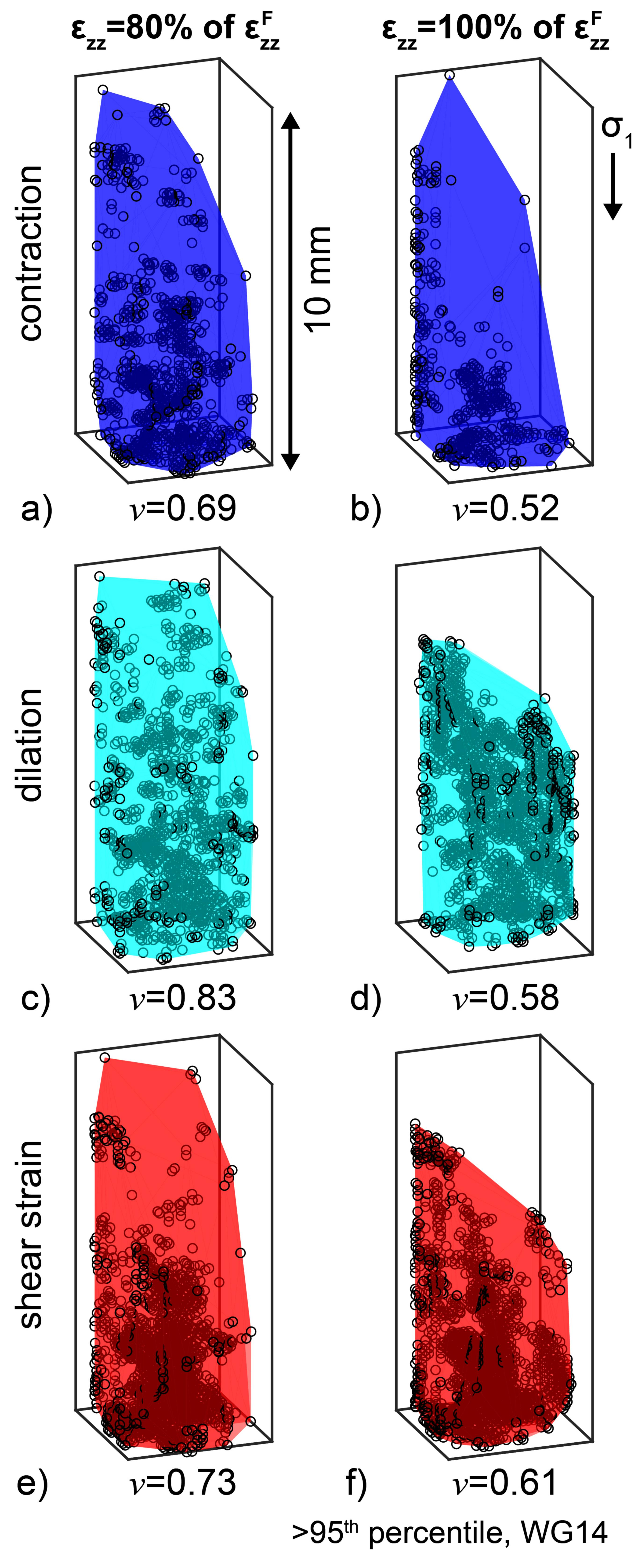


Figure 5.	
-----------	--

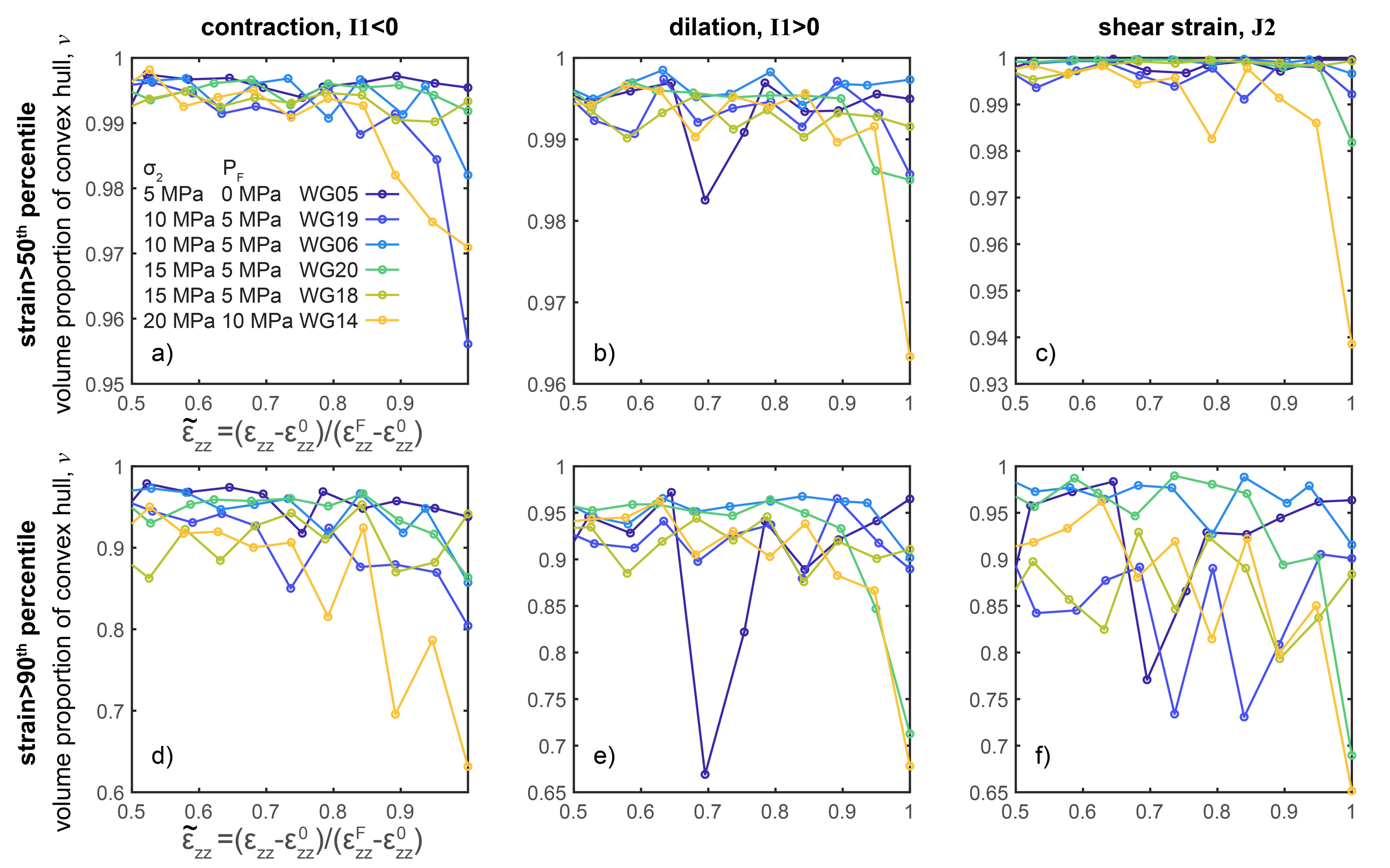


Figure 6	5.
----------	----

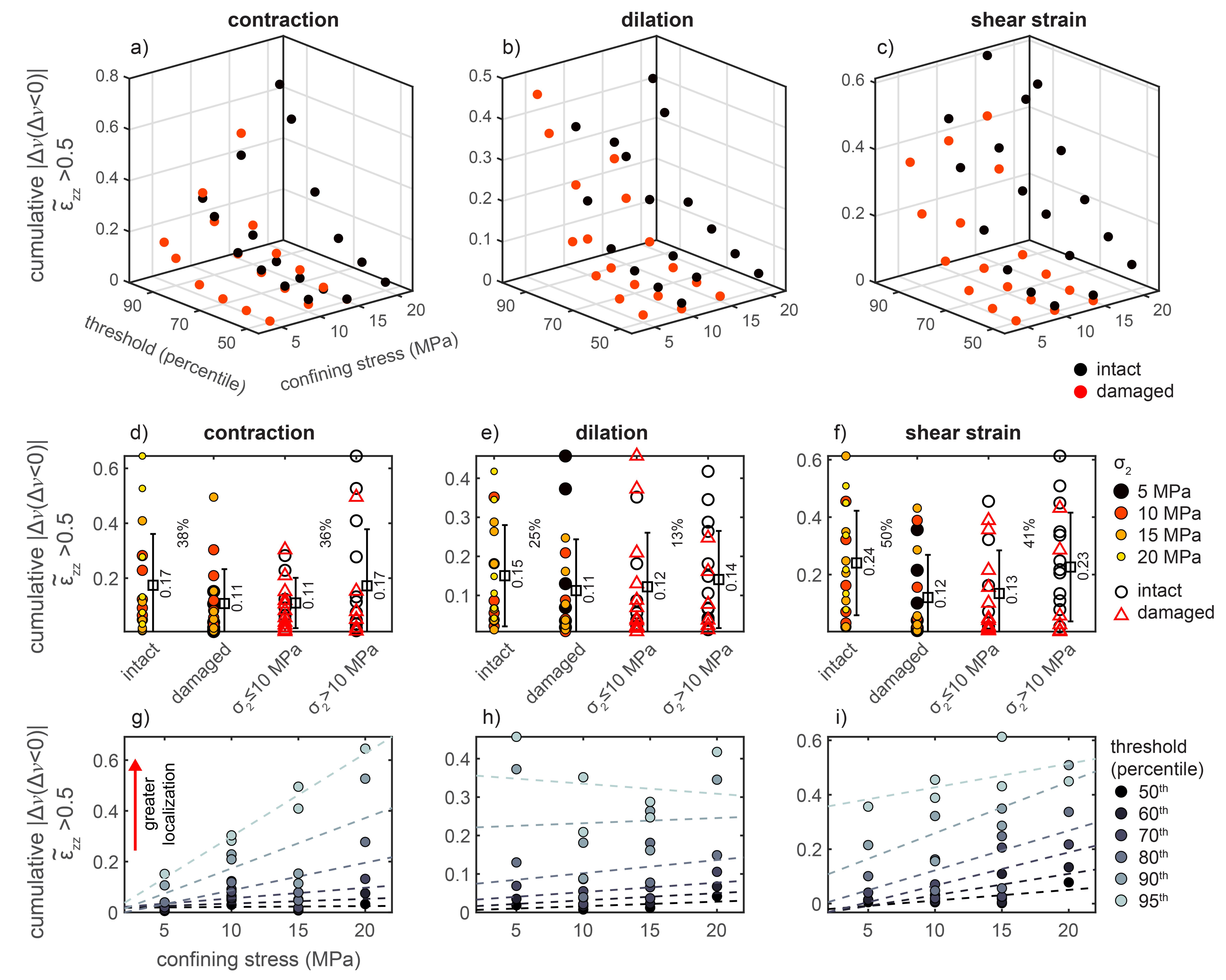


Figure 7.	
-----------	--

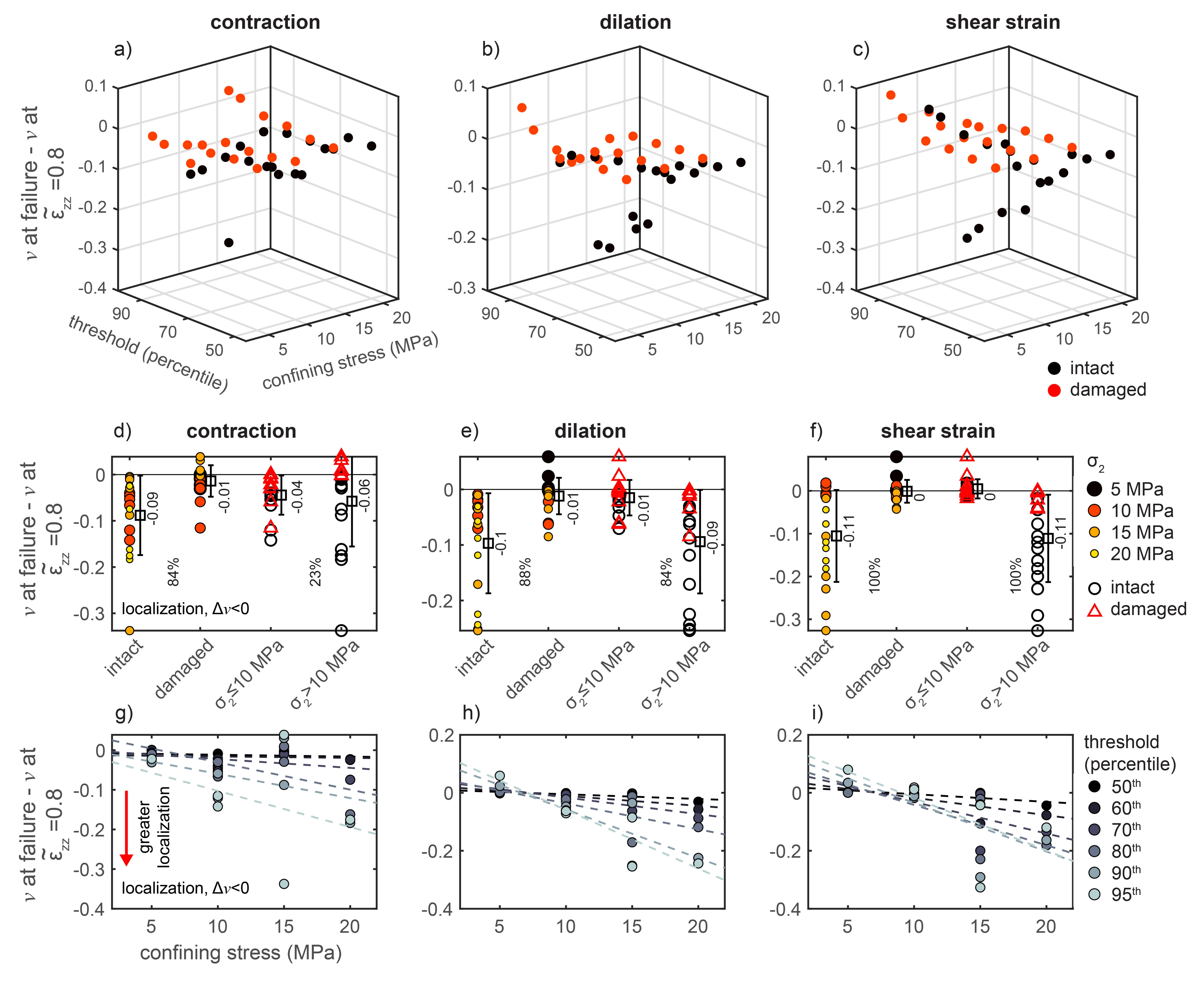


Figure 8.	
-----------	--

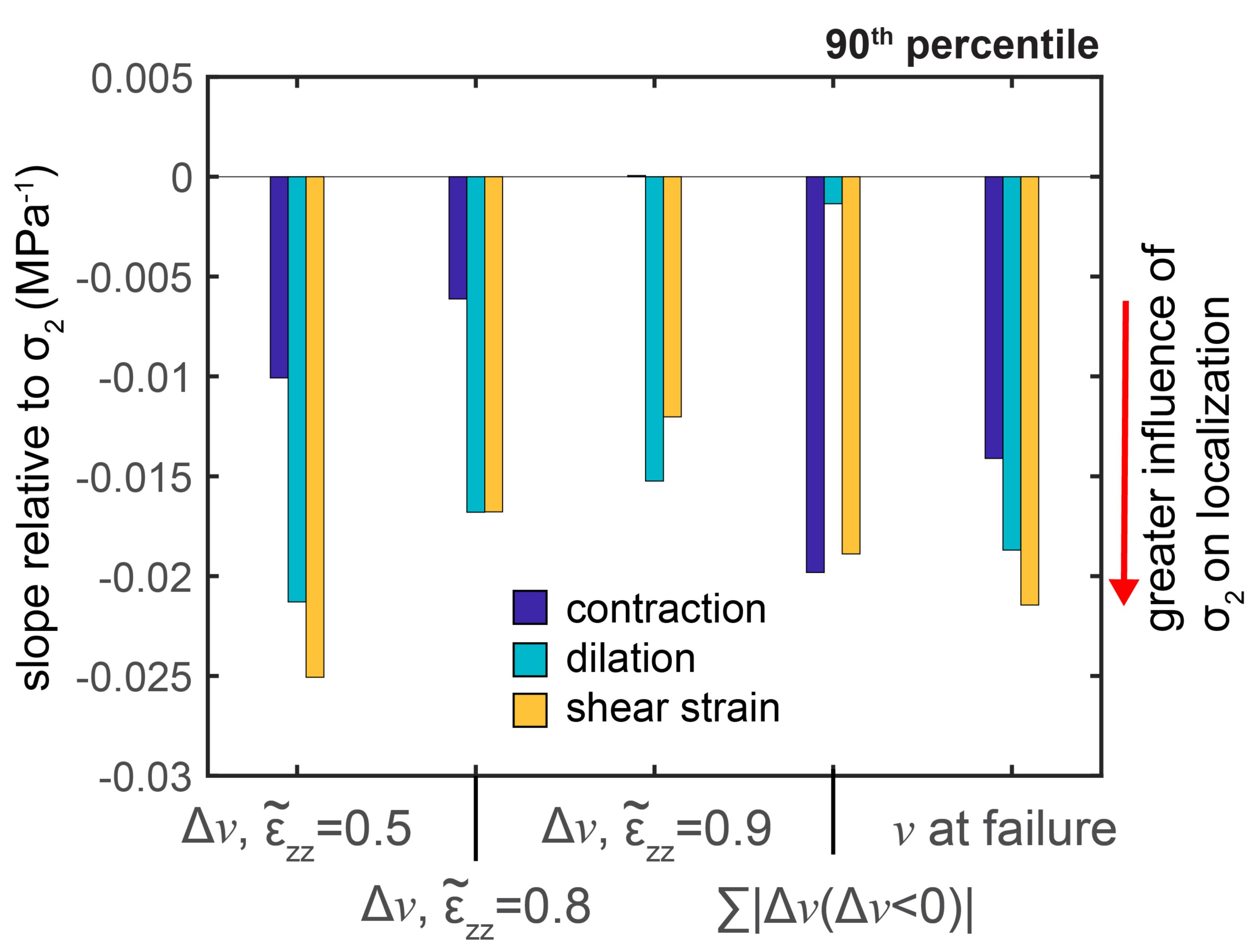


Figure 9.	
-----------	--

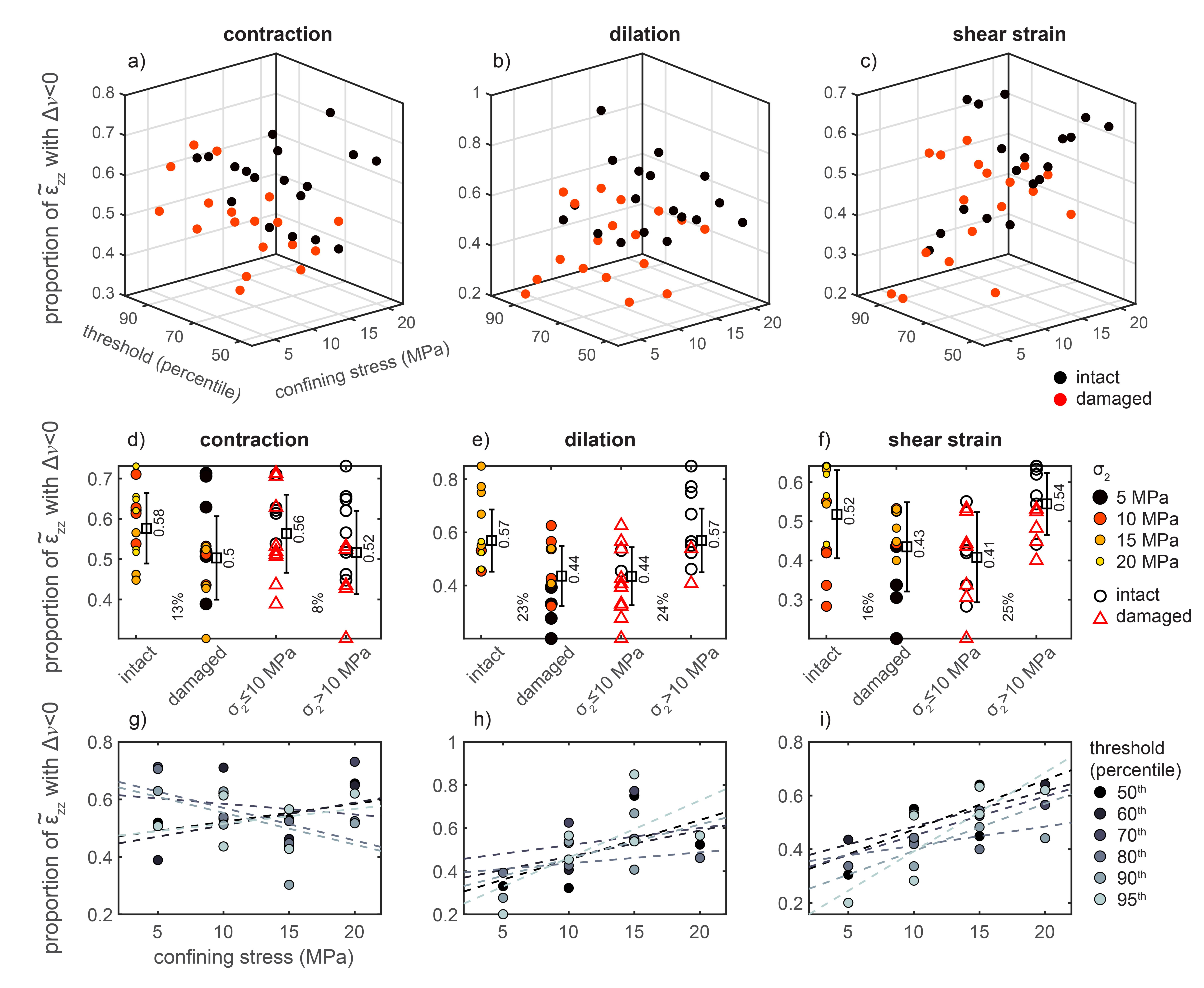
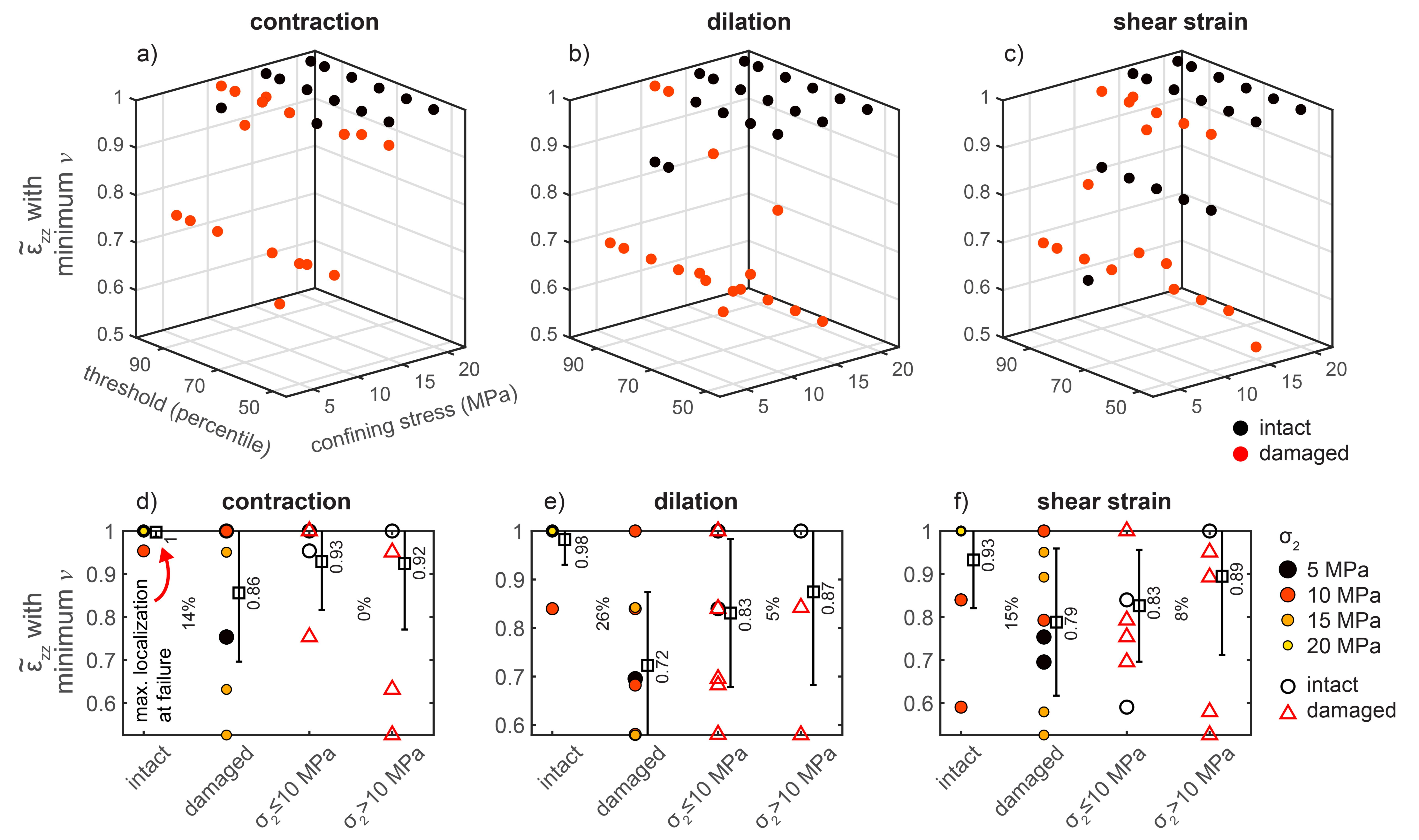


Figure	10.



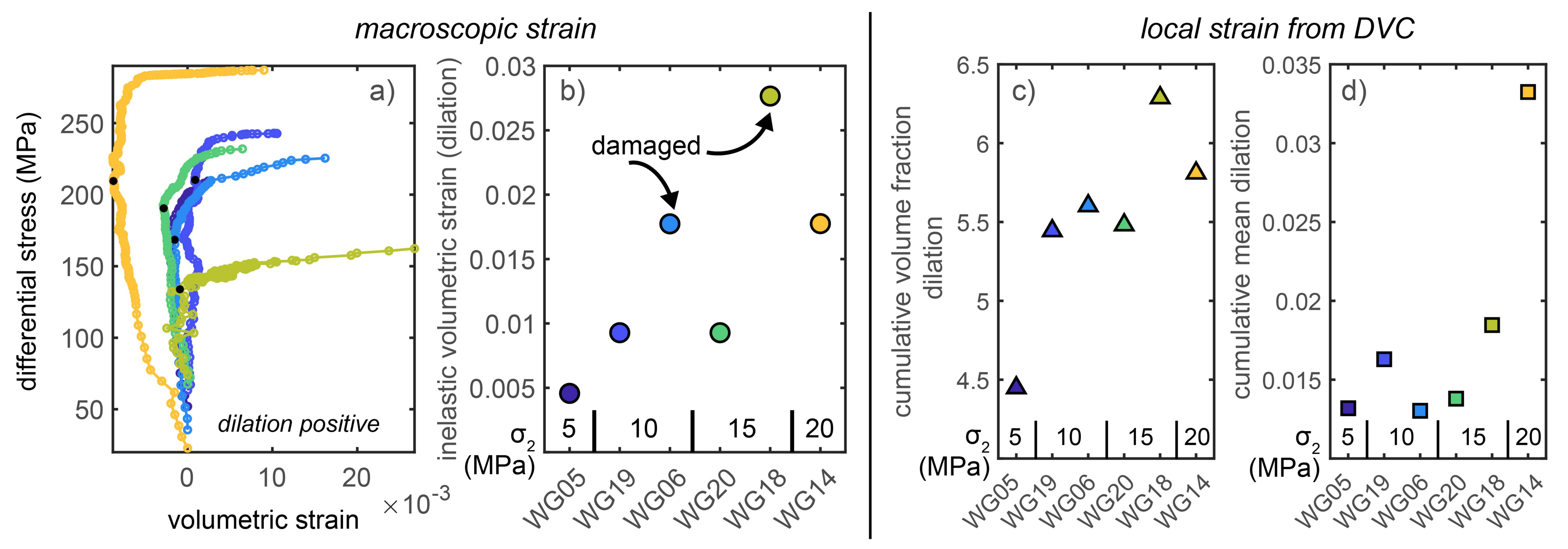
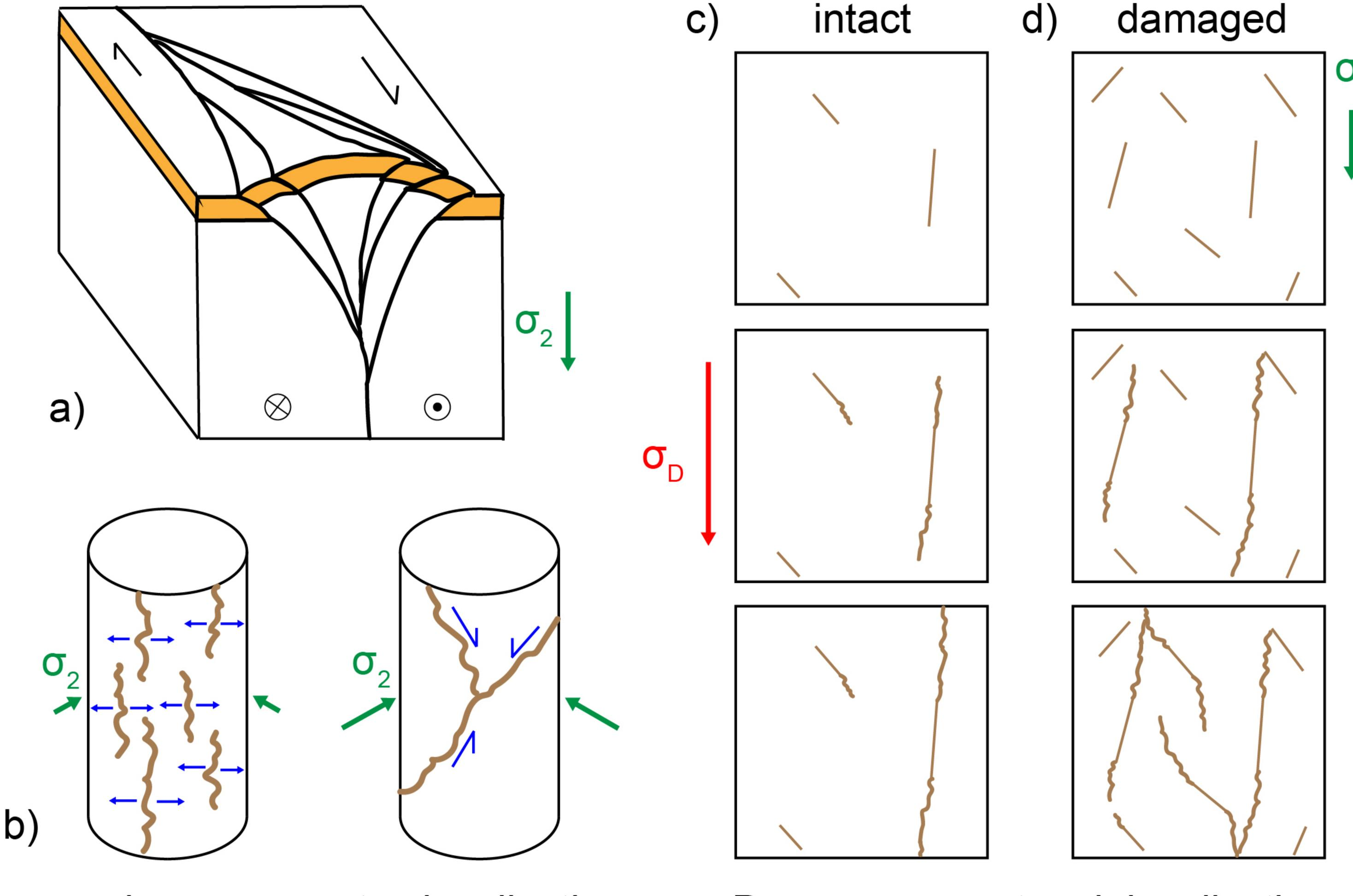


Figure	12.
--------	-----



Increasing  $\sigma_2$  promotes localization.

Damage promotes delocalization.

- 1 The influence of confining stress and preexisting damage on strain
- 2 localization in fluid-saturated crystalline rocks in the upper crust
- 3 Jessica McBeck<sup>1</sup>, Benoît Cordonnier<sup>2</sup>, Yehuda Ben-Zion<sup>3</sup>, François Renard<sup>1,4</sup>
- <sup>4</sup> Niord Centre, Departments of Physics and Geosciences, University of Oslo, Oslo, Norway.
- 5 <sup>2</sup>European Synchrotron Radiation Facility, Grenoble, France.
- 6 <sup>3</sup>Department of Earth Sciences and Southern California Earthquake Center, University of
- 7 Southern California, Los Angeles, CA, USA.
- <sup>4</sup>Université Grenoble Alpes, Université Savoie Mont Blanc, Université Gustave Eiffel,
- 9 CNRS, IRD, ISTerre, 38000 Grenoble, France.
- 10 Corresponding author: Jessica McBeck (j.a.mcbeck@geo.uio.no)
- 11 **Key Points:**
- Digital volume correlation of X-ray tomograms reveals strain localization in triaxial compression experiments.
- Larger confining stress promotes localization approaching macroscopic failure.
- More preexisting damage promotes episodes of delocalization.

### **Abstract**

16

33

48

49

50 51

52

- 17 The spatial organization of deformation may provide key information about the timing of
- catastrophic failure in the brittle regime. In an ideal homogenous system, deformation may
- 19 continually localize toward macroscopic failure, and so increasing localization
- 20 unambiguously signals approaching failure. However, recent analyses demonstrate that
- 21 deformation, including low magnitude seismicity, and fractures and strain in triaxial
- compression experiments, experience temporary phases of delocalization superposed on an
- 23 overall trend of localization toward large failure events. To constrain the conditions that
- promote delocalization, we perform a series of X-ray tomography experiments at varying
- confining stresses (5-20 MPa) and fluid pressures (zero to 10 MPa) on Westerly granite cores
- 26 with varying amounts of preexisting damage. We track the spatial distribution of the strain
- events with the highest magnitudes of the population within a given time step. The results
- 28 show that larger confining stress promotes more dilation, and promotes greater localization of
- 29 the high strain events approaching macroscopic failure. In contrast, greater amounts of
- 30 preexisting damage promote delocalization. Importantly, the dilative strain experiences more
- 31 systematic localization than the shear strain, and so may provide more reliable information
- 32 about the timing of catastrophic failure than the shear strain.

# Plain Language Summary

- 34 The ability of deformation, such as fractures and strain, to spatially cluster or localize
- produces a wide range of geologic features on Earth, such as crustal fault networks and plate
- 36 tectonics. Previous work demonstrates that deformation can evolve toward more localized
- distributions. However, recent analyses show that deformation can temporarily decrease in
- 38 localization. These decreases in localization complicate efforts to use the spatial organization
- of seismicity, for example, as a precursor of approaching large earthquakes. The factors that
- 40 promote phases of delocalization remain unconstrained. Here, we perform a series of
- 41 experiments to identify the factors that control the delocalization of local strain events within
- 42 low porosity, Westerly granite rock cores. We find that both the confining stress, indicative
- of depth within the crust, and the amount of preexisting damage of the rock cores control the
- 44 amount of localization that the strain events experience, and the phases of delocalization.
- 45 Increasing confining stress produces more localization of the high strain events. More
- 46 preexisting damage produces more delocalization.
- 47 **Key words**: localization, strain, triaxial compression, confining stress, dilation, granite

### 1 Introduction

The localization of strain along fractures, faults, and shear zones is a fundamental phenomenon of rock deformation (e.g., Rudnicki & Rice, 1975; Lockner et al., 1991; Satoh et al., 1996; Benson et al., 2007; Lyakhovsky et al., 2011; Ben-Zion & Zaliapin, 2019). The ability of deformation to localize from the micrometer- to kilometer-scale allowed the Earth's

- crust to partition into different volumes, and thus is responsible for plate tectonics (e.g.,
- 54 Gueydan et al., 2014; Mulyukova & Bercovici, 2019). Monitoring the localization of
- deformation may also be useful for recognizing the development of a preparation phase that
- leads to catastrophic failure in the upper crust, such as large magnitude earthquakes. In
- 57 particular, machine learning analyses indicate that tracking the distance between fractures in
- 58 triaxial compression experiments can help successfully predict the timing of catastrophic
- failure (McBeck et al., 2020b). Similarly, recent observations show that low magnitude
- seismicity localized in the final two to three years preceding several M>7 earthquakes in
- 61 Southern and Baja California (Ben-Zion & Zaliapin, 2020). However, for some earthquakes,
- 62 the seismicity periodically decreased in localization, or delocalized, in the several months

preceding the earthquake. These phases of delocalization obscure the relationship between macroscopic failure and localization, and thereby complicate efforts to forecast the timing of an impending large earthquake using the spatial distribution of seismicity. The factors that control whether a rock or crustal volume may experience phases of delocalization remain largely unconstrained.

To help constrain these factors, we perform a series of X-ray synchrotron tomography triaxial compression experiments and track the localization of the local three-dimensional strains calculated from digital volume correlation. To assess the influence of confining stress and effective stress on strain localization, we systematically change the confining stress from 5 MPa to 20 MPa, and fluid pressure from zero to 10 MPa in the experiments. To assess the influence of preexisting heterogeneities on localization, we introduce a network of preexisting fractures and weaknesses into several of the rock cores by thermal treatment. This set of experiments thus allows comparison of the localization of the strain events in relatively intact and damaged rocks, and in systems with lower and higher confining stress.

# 2 Methods

 2.1. X-ray tomography triaxial compression experiments

We performed six triaxial compression experiments at beamline ID19 at the European Synchrotron Radiation Facility. We used 10 mm tall and 4 mm diameter cylinders of Westerly granite, which is a low-porosity crystalline rock dominated by quartz, feldspar, and biotite. The initial porosity is lower than 1%.

We imposed a constant confining stress in each experiment (5-20 MPa), and constant pore fluid pressure (0-10 MPa) (**Figure 1**) with the Hades triaxial compression apparatus (Renard et al., 2016). We varied the confining stress and fluid pressure so that five of the experiments experienced the same effective stress, confining stress minus fluid pressure ( $P_e$ =5 MPa), and one of the experiments experienced  $P_e$ =10 MPa. **Table** S1 lists all the symbols and notations used here. We increased the axial stress in steps of 0.5-5 MPa until the rock failed with a stress drop, with smaller steps closer to failure. After each increase in axial stress, we acquired a X-ray tomogram within one and half minutes while the core was inside the deformation apparatus.

We deformed intact and heat-treated, or damaged, Westerly granite cores. The crack density produced by thermal heating depends on the temperature, differences in the thermal expansion of the minerals, initial porosity, and the grain size (e.g., Fredrich & Wong, 1986). Heating granite to temperatures above 600°C produces significant increases in the crack density and porosity, and decreases in the P-wave speed and uniaxial compressive strength (Griffiths et al., 2017). We heated the cores with an initial heating rate of 4°C/minute from room temperature to 650°C in an oven, and then for five hours at 650°C, and then with a cooling rate of 4°C/minute to room temperature. This heating procedure causes the damaged rock cores to fail at lower differential stresses than the intact rock cores for the same confining stress and effective stress conditions. We performed all the experiments at ambient room temperature in the range 22-24°C. For the experiments that include fluid pressure, we saturated the granite cores in deionized water in a vacuum chamber for two weeks before the experiment.

Following each experiment, we reconstructed the acquired radiographs into three-dimensional volumes. The three-dimensional volumes, or tomograms, are 1600x1600x1600 voxels, and each voxel side length is  $6.5~\mu m$ . The spatial resolution of the tomograms is

### manuscript submitted to JGR Solid Earth

within two to three voxel side lengths. During reconstruction, we applied methods to remove acquisition noise. We then reduced the remaining noise in the reconstructed, three-dimensional data using the software Avizo3D<sup>TM</sup>, such as a non-local means filter (Buades et al., 2005). We calculate the macroscopic axial strain done on the rock cores,  $\varepsilon_{zz}$ , using the height of the rock core identified in each tomogram. Consequently, the spatial resolution and quality of the tomogram influence the calculated  $\varepsilon_{zz}$ .

In one of the experiments on a damaged core (WG18), a system-spanning, horizontal fracture developed as the core was inserted into the deformation apparatus (**Figure S1**). With increasing axial stress, this fracture closed, and other fractures propagated throughout the core. This large preexisting fracture caused this core to fail at a lower differential stress, and to accumulate more  $\varepsilon_{zz}$  preceding macroscopic failure than expected, and than the other experiments. This experiment thus represents an endmember of rock deformation within a preexisting highly fractured system.

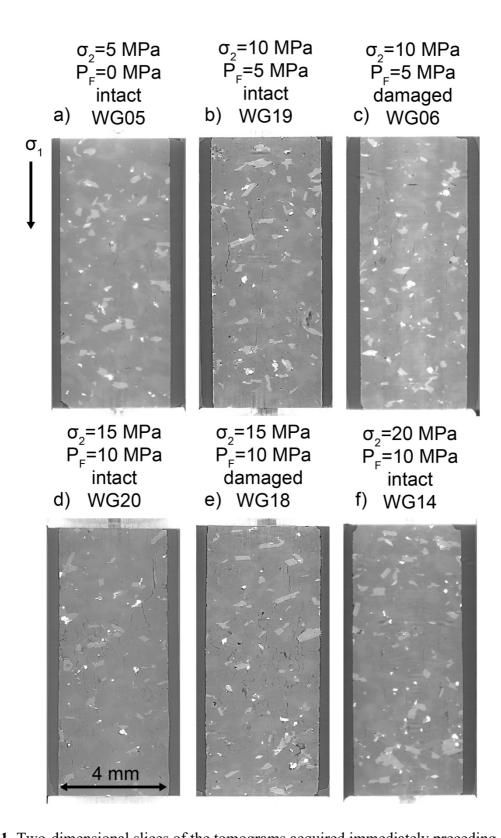


**Figure 1**. Two-dimensional slices of the tomograms acquired immediately preceding macroscopic failure in the six experiments. Minerals with larger densities, such as oxides and biotite, have larger gray-scale values in the tomograms (lighter gray and white regions), than minerals with lower densities, such as quartz and feldspar (darker gray). The fractures have lower gray-scale values (dark gray and black). The applied confining stress,  $\sigma_2$ , and fluid pressure,  $P_F$ , and whether the rock core was damaged or intact are listed above each slice.

## 2.2. Digital volume correlation analysis

To calculate the local three-dimensional strain fields, we used the software TomoWarp2 (Tudisco et al., 2017). Digital volume correlation analyses search for similar patterns of voxels in pairs of three-dimensional images and then calculate the displacement vector that maps a pattern in one image to a pattern in another image (e.g., Charalampidou et al., 2011). In TomoWarp2, the node spacing and correlation window size determine the spatial resolution and the size of the volume used to identify similar patterns of voxels, respectively. Calculations with a node spacing of 20 voxels (0.13 mm) and correlation window size of 10 voxels (65  $\mu$ m) produce an acceptable spatial resolution and reasonable levels of signal to noise (McBeck et al., 2018).

To identify the tomograms used in the digital volume correlation analysis, we divide each experiment into 20 equal increments of the macroscopic axial strain,  $\varepsilon_{zz}$ , and then identify the tomograms with the closest  $\varepsilon_{zz}$  to the specified increments (Figure 2), following our previous analyses (e.g., McBeck et al., 2018). We then use these pairs of tomograms to perform 19 digital volume correlation calculations for each experiment. The reported strain tensors are thus the local, incremental strains done between each tomogram acquisition, and not the total cumulative strain over the entire experiment. To quantify the localization of the volumetric and deviatoric components of the strain field, we calculate the divergence, I1, (volumetric strain, contractive, I1 < 0, and dilative, I1 > 0) and the second invariant of the deviatoric strain tensor, 12, (deviatoric strain, shear) from the incremental displacement fields. In previous analyses, we used the curl of the displacement field to characterize the shear strain, following the technique of the geodetic community (McBeck et al., 2019, 2020c). However, recent machine learning analyses suggest that 12 may provide more information about the timing of fault reactivation and macroscopic failure in strike-slip fault systems than the curl of the displacement field (McBeck et al 2022a). We also use 12 to characterize the shear strain because it determines the maximum distortion criterion, or von Mises yield criterion. Because each tomogram captures regions outside the rock core, such as the jacket and deformation apparatus, we remove the portion of the calculated strain field that is outside the rock core.

128

129

130

131

132

133

134

135

136

137

138

139

140

141142

143144

145

146

147

148

149150

151

152

153

154

155

156

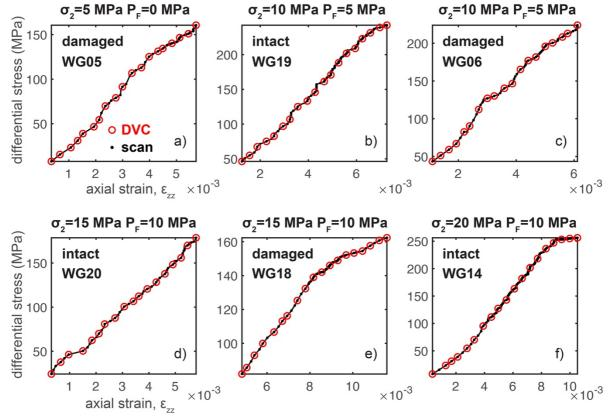


**Figure 2**. Differential stress and cumulative axial strain,  $\varepsilon_{zz}$ , when each tomogram or scan was acquired (black symbols) and the conditions of the scans used in the digital volume correlation (DVC) analyses (red symbols) for each experiment. The applied confining stress,  $\sigma_2$ , fluid pressure,  $P_F$ , and whether the core was heat-treated (damaged) before the experiment or not (intact) are listed at the top of each plot. The differential stress and  $\varepsilon_{zz}$  of the first scans shown here are not zero because we do not show the scans that were acquired during the early phase of each experiment when the axial strain-differential stress curve is highly non-linear and concave upward. This non-linearity is caused in part by the closure of preexisting fractures and pores, and to a larger extent by the settling of the rock core inside the apparatus as it comes in contact with the upper and lower pistons. We only include the scans following this non-linear stage in the digital volume correlation analysis.

#### 3 Results

## 3.1. Evolution of the spatial localization of the strain components

To quantify the spatial localization of the contraction, |I1 < 0|, dilation, I1 > 0, and shear strain, I2, we compare the volume of the polyhedron that surrounds high values of each strain component,  $v_h$ , to the volume of the polyhedron that surrounds all of the values of the given strain component,  $v_t$ . For the shear strain,  $v_t$  is equal to the volume of the rock core used in the digital volume correlation analysis. For the volumetric strain components,  $v_t$  may be smaller than the volume of the rock core because the fraction of the rock core occupied by the dilation or contraction evolves throughout the experiment. Consequently, we first examine the evolution of this volume,  $v_t$ , divided by the volume of the total rock used in the digital volume correlation analysis for the dilation and contraction throughout each experiment. This comparison also provides insight into the influence of confining stress,  $\sigma_2$ , on volumetric strain.

We report the time in the experiments using the normalized cumulative macroscopic axial strain,  $\widetilde{\varepsilon_{zz}}$ . We normalize the macroscopic axial strain so that the maximum and minimum values are one and zero. In particular,  $\widetilde{\varepsilon_{zz}}$  is calculated from the  $\varepsilon_{zz}$  calculated for the given tomogram, the  $\varepsilon_{zz}$  of the tomogram acquired immediately preceding macroscopic failure,  $\varepsilon_{zz}^F$ , and the  $\varepsilon_{zz}$  of the first tomogram acquired at the onset of the linear phase early in loading,  $\varepsilon_{zz}^0$ , as  $\widetilde{\varepsilon_{zz}} = (\varepsilon_{zz} - \varepsilon_{zz}^0)/(\varepsilon_{zz}^F - \varepsilon_{zz}^0)$ .

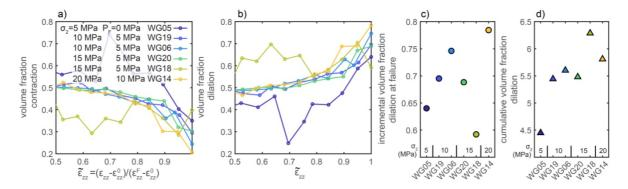
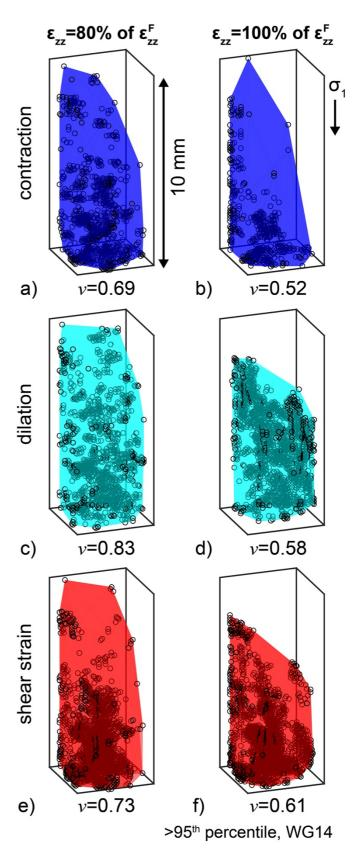


Figure 3. Fraction of the volume of the rock occupied by contraction, I1 < 0 (a) and dilation, I1 > 0 (b) as a function of the normalized cumulative macroscopic axial strain,  $\varepsilon_{zz}$ , of the second tomogram used in each digital volume correlation calculation, and the incremental (c) and sum of the incremental, or cumulative, fraction occupied by dilation (d) at the end of each experiment. The normalized cumulative macroscopic axial strain,  $\varepsilon_{zz}$ , is a function of the  $\varepsilon_{zz}$  calculated from the given tomogram, the  $\varepsilon_{zz}$  of the tomogram acquired immediately preceding macroscopic failure,  $\varepsilon_{zz}^F$ , and the  $\varepsilon_{zz}$  of the first tomogram acquired at the onset of the linear phase early in loading,  $\varepsilon_{zz}^0$ , as  $\widetilde{\varepsilon_{zz}} = (\varepsilon_{zz} - \varepsilon_{zz}^0)/(\varepsilon_{zz}^F - \varepsilon_{zz}^0)$ . The colors of the symbols indicate different experiments.

The volume fraction occupied by contraction generally decreases while the fraction occupied by dilation generally increases after about  $0.8 \ \tilde{\epsilon}_{zz}$  (**Figure 3**). The exception to this trend is experiment WG18. This experiment hosts relatively large volume fractions of dilation, up to 0.7, early in loading, when  $\tilde{\epsilon}_{zz}$  is about 0.6. This experiment may have unique behavior because as this rock core was loaded into the deformation apparatus, it developed a core-spanning fracture perpendicular to the maximum compressive stress (**Figure S1**). Increasing axial stress during the experiment then closed the fracture.

To assess the influence of  $\sigma_2$  on the volumetric strains, we compare the incremental volume fraction occupied by dilation immediately preceding failure, derived from the final digital volume correlation calculation, and the sum of the incremental (cumulative) volume fraction from the onset of loading to the end of the experiment. Both the incremental and cumulative strains indicate that larger  $\sigma_2$  promotes dilation (**Figure 3c**, **d**). Experiment WG14, with the largest confining stress ( $\sigma_2$ =20 MPa) and largest effective stress ( $P_e$ =10 MPa), achieves the largest incremental volume fraction occupied by dilation at the end of the experiment, and immediately preceding failure (**Figure 3c**), and the second largest cumulative volume fraction (**Figure 3d**). Experiment WG05, with the smallest  $\sigma_2$  (5 MPa), and smallest  $P_e$  (5 MPa), achieves the smallest cumulative and second smallest incremental volume fraction occupied by dilation at the end of the experiment. Experiment WG18, with  $\sigma_2$ =15 MPa and  $P_e$ =5 MPa, experiences the smallest incremental volume fraction and largest cumulative volume fraction occupied by dilation. The development of the core-spanning fracture produced a relatively high volume fraction of dilation earlier in loading in this experiment compared to the other experiments. In general, greater  $\sigma_2$  and  $P_e$  promote dilation.

221 Figure 4. Spatial distribution of 222 the high values (>95<sup>th</sup> percentile) 223 of the contraction (a, b), dilation 224 (c, d) and shear strain (e, f) at  $\varepsilon_{zz}/\varepsilon_{zz}^F$ =0.80 (a, c, e), and at  $\varepsilon_{zz}/\varepsilon_{zz}^F$ =1, immediately preceding 225 226 macroscopic failure (b, d, f) for 227 experiment WG14. Black circles 228 229 show the location of the three-230 dimensional strain field with high 231 values of incremental strain, >95<sup>th</sup> 232 percentile. Shaded dark blue, light 233 blue and red areas show the 234 convex hull that fits around the 235 high strain values. The numbers 236 below each plot show the fraction 237 of the volume of the convex hull 238 relative to the total volume 239 occupied by all of the values of the strain component, v. The v of the 240 contraction, dilation, and shear 241 242 strain all decrease with increasing 243 differential stress, from 80% to 244 100% of  $\varepsilon_{zz}^F$ .



As described above, we calculate the volume of the convex hull or polyhedron that surrounds the population of the high strains,  $v_h$ , for each of the 19 digital volume correlation calculations performed in each experiment in order to quantify the spatial localization of the high strain values. We use this metric, rather than a previous metric we used to quantify the localization of strain (McBeck et al., 2022b), because this metric does not require defining a grid size, and thus the results are independent of this parameter. We report  $v_h$  divided by the volume of the polyhedron that surrounds all of the values of the given strain component,  $v_t$ , as  $v = v_h/v_t$ . Figure 4 shows the polyhedrons and resulting v found for the contractive, dilative, and shear strain values greater than the 95<sup>th</sup> percentile value at two different time steps (and digital volume correlation calculations) in experiment WG14. One of the time steps occurs immediately preceding macroscopic failure, when the  $\varepsilon_{zz}$  of the second tomogram used in the digital volume correlation analysis is equal to the  $\varepsilon_{zz}$  of the final tomogram acquired in the experiment,  $\varepsilon_{zz}^F$ , or  $\varepsilon_{zz}/\varepsilon_{zz}^F = 1$ . The other time step is earlier in the experiment, when  $\varepsilon_{zz}/\varepsilon_{zz}^F = 0.8$ . These example polyhedrons show that the v of each strain component decreases with increasing differential stress and cumulative axial strain, indicative of localization towards macroscopic failure.

**Figure 5** shows v for each strain component and all of the experiments for two of the percentile thresholds used to identify the high strain values, the  $50^{th}$  and  $90^{th}$  percentile. We perform the analyses with six different thresholds ( $50^{th}$ ,  $60^{th}$ ,  $70^{th}$ ,  $80^{th}$ ,  $90^{th}$ ,  $95^{th}$ ), and summarize those results in subsequent sections. When the dilation or contraction are greater than the  $50^{th}$  or  $90^{th}$  percentile, all but one or two experiments (WG05 and WG18) host decreases in v after about 0.8 to 0.9  $\varepsilon_{zz}$ . For the shear strain, a smaller number of the experiments host decreases in v toward failure. The decreasing v indicates that the high strain events localize. We next quantify these decreases in v approaching macroscopic failure.

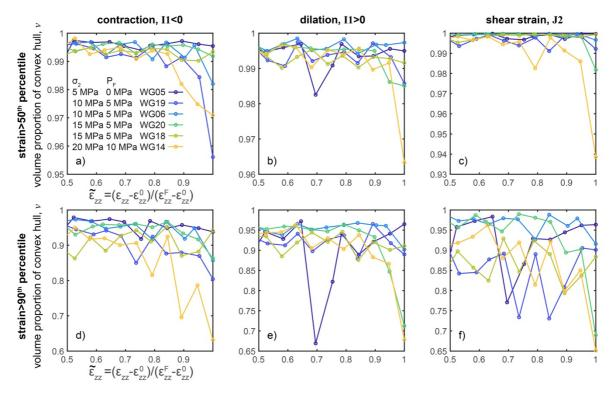


**Figure 5**. Evolution of the volume fraction of the convex hull around the high strain values, v, for strains greater than the  $50^{th}$  percentile (a-c) and  $90^{th}$  percentile (d-f), for the absolute

value of the contraction, |I1 < 0|, (a, d) dilation, I1 > 0, (b-e) and shear strain, I3 (c, f). The different colors of the curves correspond to the different experiments.

To quantify the evolution of v, we first examine the cumulative localization approaching macroscopic failure. **Figure 6** shows the absolute value of the sum of the negative values of the change in v from one digital volume correlation calculation to the next, when  $\widetilde{\varepsilon_{zz}} > 0.5$ ,  $\sum_{\widetilde{\varepsilon_{zz}} = 0.5}^{\widetilde{\varepsilon_{zz}} = 1} |\Delta v(\Delta v < 0)|$ . Negative  $\Delta v$  indicates that the volume of the polyhedron that surrounds the high strain events decreases from one digital volume correlation calculation to the next, and thus the high strain events localize from one stress step to the next. We sum the values when  $\widetilde{\varepsilon_{zz}} > 0.5$ , and not from the onset of loading, because we aim to characterize strain localization approaching macroscopic failure. Larger values of the cumulative localization thus indicate greater magnitudes of localization toward macroscopic failure.

The cumulative localization increases with the strain threshold (**Figure 6**). The analysis thus detects more localization with larger strain thresholds. This trend is expected because larger strain thresholds produce lower numbers of high strain events. The cumulative localization increases with  $\sigma_2$  for the contraction, dilation, and shear strain for all of the thresholds  $<95^{th}$  percentile (**Figure 6g-i**). When the threshold is the  $95^{th}$  percentile, the cumulative localization increases with  $\sigma_2$  for the contraction and shear strain, but not the dilation (**Figure 6h**). Dividing the experiments into groups with relatively lower and higher  $\sigma_2$  helps show that the cumulative localization increases with  $\sigma_2$  (**Figure 6d-f**). Using all of the thresholds, the mean of the cumulative localization of the contraction for the experiments with  $\sigma_2 > 10$  MPa is 36% greater than the mean of the experiments with  $\sigma_2 \leq 10$  MPa. This difference is 13% and 41% for the dilation and shear strain, respectively. The generally positive slopes of the lines that fit through the cumulative localization and  $\sigma_2$  for each strain component and each threshold also indicate that larger  $\sigma_2$  produces greater cumulative localization.

The results reveal differences in the cumulative localization of the nominally intact rocks and heat-treated, damaged rocks (**Figure 6d-f**). The intact rocks tend to experience more cumulative localization than the damaged rocks. In particular, the mean of the cumulative localization of the intact rocks is 38%, 25%, and 50% greater than the mean of the damaged rocks for the contraction, dilation, and shear strain, respectively.

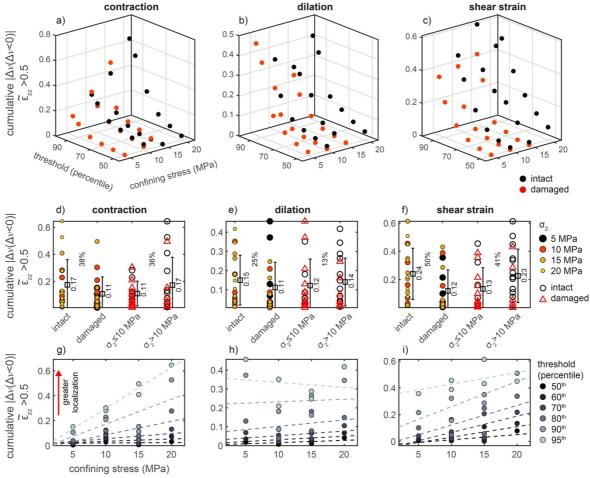


Figure 6. The cumulative localization hosted by each strain component approaching failure, calculated as the sum of the absolute value of the negative change in v when  $\widetilde{\varepsilon_{zz}} > 0.5$ ,  $\sum_{\widetilde{\varepsilon_{ZZ}}=0.5}^{\widetilde{\varepsilon_{ZZ}}=1} |\Delta v(\Delta v < 0)|$ . Negative  $\Delta v$  indicates that the volume of the polyhedron that surrounds the high strain events decreases from one digital volume correlation calculation to the next, and thus the high strain events localize from one stress step to the next. The top row (a-c) shows three-dimensional plots of the cumulative localization as a function of the applied confining stress,  $\sigma_2$ , and the thresholds used to identify the high strains for the contraction (a), dilation (b), and shear strain (c). The black and red symbols indicate if the sample was intact (black) or damaged (red). The second row (d-f) shows the cumulative localization grouped by the intact and damaged rocks, and experiments with lower  $\sigma_2$  ( $\leq 10$  MPa) and higher  $\sigma_2$  (>10 MPa). The color and size of the symbols indicate the  $\sigma_2$  for the grouping of the intact and damaged rocks. The black circles and red triangles indicate if the sample was intact (black) or damaged (red) for the grouping of the lower and higher  $\sigma_2$ . The square symbols and error bars show the mean  $\pm$  one standard deviation of each group of data points. The number next to each error bar lists the mean. The percentages between each pair of groups shows the percentage difference between the magnitude of the larger mean,  $\mu_{max}$ , and smaller mean,  $\mu_{min}$ , as  $(\mu_{max} - \mu_{min})/\mu_{max}$ . The third row (g-i) shows the cumulative localization as a function of  $\sigma_2$ . The color of the symbols indicates the threshold used to identify the high strain values. The dashed lines show the fit of the linear function through the data derived from each threshold. The intact rocks localize by larger amounts than the damaged rocks. Experiments with larger confining stress generally host more localization than experiments with lower confining stress.

304

305

306

307

308

309

310311

312

313

314

315316

317

318319

320

321

322

323

324

#### manuscript submitted to JGR Solid Earth

We also examine alternative methods of quantifying the evolution of v approaching macroscopic failure, in addition to the cumulative localization (**Figure 6**). **Figure 7** shows the localization preceding macroscopic failure measured using the difference in v from the final tomogram acquired immediately preceding failure, when  $\widetilde{\varepsilon_{zz}}$  is one, and when  $\widetilde{\varepsilon_{zz}}$  is 0.8,  $\Delta v$ . Negative  $\Delta v$  indicates that the high strain events localize towards macroscopic failure. **Figure S2** and **Figure S3** show the  $\Delta v$  calculated using  $\widetilde{\varepsilon_{zz}}$  of 0.5 and using  $\widetilde{\varepsilon_{zz}}$  of 0.9, which produce similar results to those reported for when  $\widetilde{\varepsilon_{zz}}$  is 0.8.

Using all of the tested combinations of strain components, experiments, high strain thresholds, and selected  $\widetilde{\varepsilon_{zz}}$ ,  $\Delta v$  is negative in 75% of the tested combinations. This high rate indicates that the vast majority of strain components localize toward failure. However, this rate varies among the different strain components. For the dilation and contraction,  $\Delta v$  is negative in 80% of the tested combinations. For the shear strain, in contrast,  $\Delta v$  is negative in only 67% of the tested combinations. Consequently, the volumetric strain components are more likely to experience localization approaching macroscopic failure than the shear strain.

The trends observed in this localization metric (**Figure 7**, **Figure S2**, **Figure S3**) are similar to those observed for the cumulative localization (**Figure 6**). The amount of localization increases with the high strain threshold and  $\sigma_2$ , producing increasingly negative  $\Delta v$  (**Figure 7g-i**). Consequently, the experiments with higher  $\sigma_2$  localize more than the experiments with lower  $\sigma_2$ . In addition, the intact rocks localize more than the damaged rocks. The trends observed here also occur when we calculate  $\Delta v$  using  $\widetilde{\varepsilon_{zz}}$ =0.5, and  $\widetilde{\varepsilon_{zz}}$ =0.9 (**Figure S2**, **Figure S3**), and for the v observed in the final digital volume correlation calculation, which captures the strain field immediately preceding macroscopic failure (**Figure S4**).

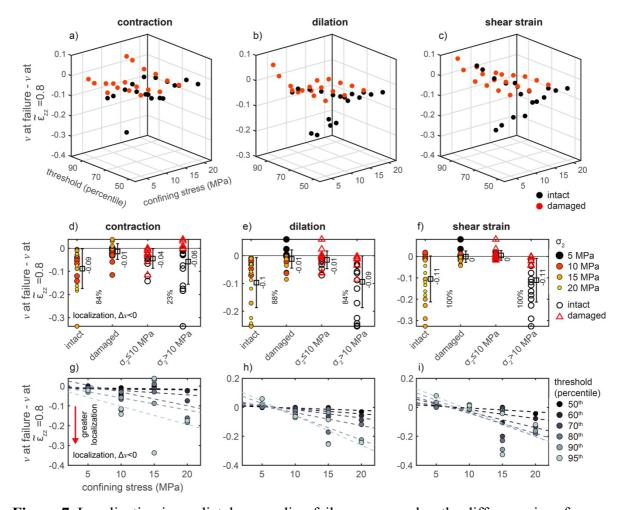


**Figure 7**. Localization immediately preceding failure measured as the difference in v from the final tomogram acquired immediately preceding failure, when  $\widetilde{\varepsilon_{zz}}$  is one, and when  $\widetilde{\varepsilon_{zz}}$  is 0.8,  $\Delta v$ . Negative  $\Delta v$  indicates that the high strain events localize towards macroscopic failure. The format of the figure is the same as **Figure 6**. The intact rocks experience larger amounts of localization preceding macroscopic failure, more negative  $\Delta v$ , than the damaged rocks. The experiments with larger confining stress host more localization than experiments with lower confining stress.

To compare the influence of  $\sigma_2$  on localization, we now report the slope of the line that fits  $\sigma_2$  and 1)  $\Delta v$  from  $\widetilde{\varepsilon_{zz}}$ =0.5, 0.8 or 0.9 to macroscopic failure, 2) the cumulative localization, and 3) v at the end of each experiment (**Figure 8**). These slopes approximate the influence of  $\sigma_2$  on localization near failure for each strain component. **Figure 6**, **Figure 7**, and **Figures S2-S4** show these lines. **Figure S5** shows the slopes derived from all the strain thresholds, and **Figure 8** shows the slopes derived using a threshold of the 90<sup>th</sup> percentile. Higher percentile thresholds produce larger slopes (**Figure S5**), and so we focus on one percentile here in order to highlight the trends observed for the other percentiles.

For each of the localization metrics except the cumulative localization, the dilation and shear strain produce larger negative slopes than the contraction (**Figure 8**). This result indicates that  $\sigma_2$  has a stronger influence on the amount of localization near failure for the dilation and shear strain than the contraction. For the cumulative localization, the slopes of the shear strain and contraction are more negative than the slope of the dilation, indicating that  $\sigma_2$  has a weaker influence on the amount of cumulative localization approaching failure

for the dilation than the shear strain or contraction. The relative magnitudes of the slopes of the cumulative localization may differ from the slopes of the other metrics because the cumulative localization of the experiment WG05, with the lowest  $\sigma_2$ , is similar to the cumulative localization of the experiments with higher  $\sigma_2$ . The large and sudden decrease in v for the dilation at  $\widetilde{\varepsilon_{zz}}$  of 0.7 produces large cumulative localization for experiment WG05 relative to the other experiments with lower  $\sigma_2$  (**Figure 5**). This temporary decrease in v, however, does not produce similarly anomalous values of  $\Delta v$  calculated using  $\widetilde{\varepsilon_{zz}}$  of 0.5, 0.8 and 0.9, or the v at macroscopic failure. Consequently, the other localization metrics are not influenced by this temporary decrease, and in general,  $\sigma_2$  has a larger influence on the dilation and shear strain than the contraction.

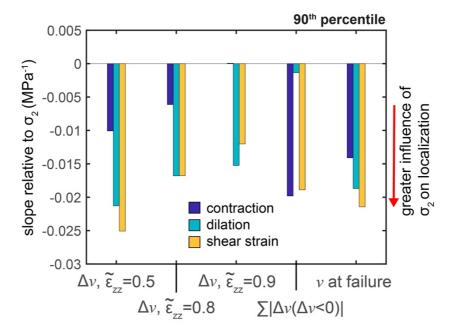


**Figure 8.** Slopes of the linear fit of different localization metrics for strains >90<sup>th</sup> percentile and  $\sigma_2$  of the experiments for each strain component: contraction (dark blue), dilation (light blue), and shear strain (yellow). The horizontal axis indicates the localization metrics: 1-3)  $\Delta v$  using  $\widetilde{\varepsilon_{zz}}$ =0.5,  $\widetilde{\varepsilon_{zz}}$ =0.8, and  $\widetilde{\varepsilon_{zz}}$ =0.9, 4) the cumulative localization, and 5) v at failure. The slopes derived from the cumulative localization were multiplied by negative one so that larger negative values indicate a stronger influence of  $\sigma_2$  on localization for all the metrics. The lines that produce each slope are shown in **Figure 6**, **Figure 7**, **Figure S2**, **Figure S3**, and **Figure S4**. In all but one of the localization metrics, the  $\sigma_2$  has a larger influence on the dilation and shear strain than the contraction.

### 3.2. Phases of delocalization and localization

The previous section focuses on the change in localization preceding macroscopic failure. Here, we compare the proportion of the experiment time, in terms of  $\widetilde{\varepsilon_{zz}}$ , that each strain component is localizing, and the timing of when the maximum localization occurs relative to macroscopic failure. In an ideal system that lacks significant heterogeneities, one may expect that the high strain values would continually localize with increasing axial strain or differential stress (Lyakhovsky et al., 2011). Consequently, the proportion of  $\widetilde{\varepsilon_{zz}}$  in which the  $\Delta v$  from one digital volume correlation calculation to the next is less than zero should be one. However, for all of the tested strain thresholds, strain components, and experiments, this proportion is always less than one, indicating that the high strains experience temporary

episodes of delocalization (**Figure 9**). The intact rocks tend to experience localization for a longer proportion of  $\widetilde{\varepsilon_{zz}}$  than the damaged rocks (**Figure 9d-f**). On average, the intact rocks experience localization for 13% (contraction), 23% (dilation), and 16% (shear strain) more  $\widetilde{\varepsilon_{zz}}$  than the damaged rocks. Thus, the damaged rocks have longer total phases of delocalization than the intact rocks.

For the dilation and shear strain, the experiments with higher  $\sigma_2$  tend to host localization for a longer period of  $\widetilde{\varepsilon_{zz}}$  than the experiments with lower  $\sigma_2$ . The experiments with  $\sigma_2 > 10$  MPa host localization on average for 24% (dilation) and 25% (shear) more  $\widetilde{\varepsilon_{zz}}$  than the experiments with  $\sigma_2 \leq 10$  MPa (**Figure 9f**). For the contraction, the experiments with  $\sigma_2 \leq 10$  MPa host slightly longer periods of  $\widetilde{\varepsilon_{zz}}$  with localization (8%) than the experiments with  $\sigma_2 > 10$  MPa.

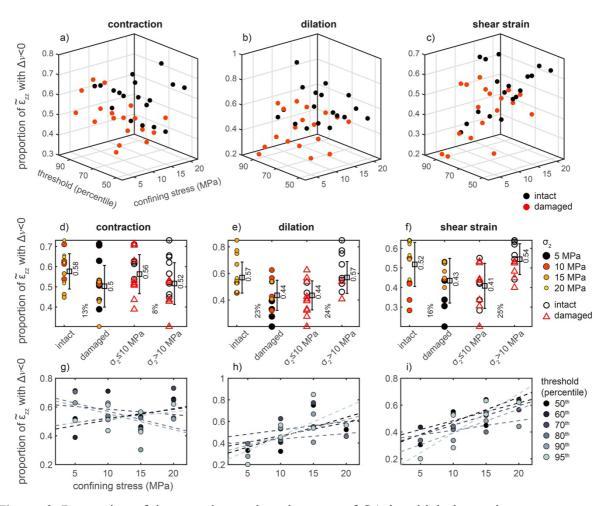
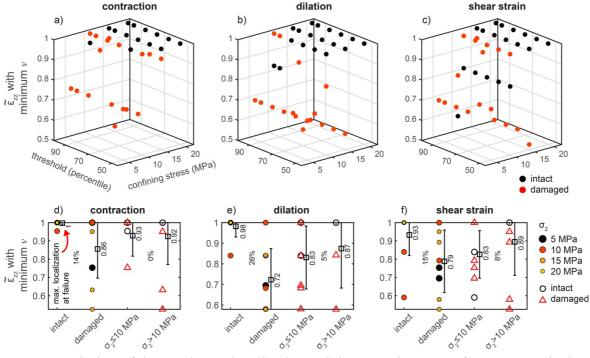


Figure 9. Proportion of the experiment time, in terms of  $\widetilde{\varepsilon}_{zz}$ , in which the strain component produces negative  $\Delta v$ , and thus localizes. Format is the same as Figure 6. The intact rocks experience larger proportions of  $\widetilde{\varepsilon}_{zz}$  in which the strain components localize than the damaged rocks. The experiments with larger confining stress generally host more  $\widetilde{\varepsilon}_{zz}$  in which the strain components localize.

These results indicate that the high strain values do not systematically increase in localization with increasing differential stress or axial strain. Instead, they experience episodes of delocalization, rather than a continuous increase or acceleration of localization toward catastrophic failure. **Figure 10** shows the  $\widetilde{\varepsilon_{zz}}$  when each strain component

experiences its minimum v, and thus maximum localization. The damaged rocks host their maximum localization earlier in loading than the intact rocks (**Figure 10d-f**). The maximum localization occurs on average at  $\widetilde{\epsilon_{zz}}$  of 0.86, 0.72, and 0.79 for the contraction, dilation and shear strain, respectively, of the damaged rocks. In contrast, for the intact rocks, the maximum localization occurs on average at  $\widetilde{\epsilon_{zz}}$  of 1, 0.98, and 0.93 for the contraction, dilation and shear strain, respectively. The differences in  $\sigma_2$  produce only small differences in the timing of the maximum localization.



**Figure 10**. Timing of the maximum localization, minimum v, in terms of  $\widetilde{\varepsilon_{zz}}$ . Format is the same as **Figure 6** (a-f). The intact rocks tend to host their maximum localization immediately preceding failure, when  $\widetilde{\varepsilon_{zz}}$  is one. In contrast, the damaged rocks host their maximum localization earlier in loading.

#### 4 Discussion

## 4.1. The influence of confining stress on volumetric strain

Tracking the volume of the rock occupied by dilation in the experiments on damaged and intact rocks, at confining stresses of 5-20 MPa, and effective stresses of 5 MPa and 10 MPa indicates that the volume of rock that experiences dilation generally increases toward failure, particularly after about  $0.8 \ \tilde{\epsilon}_{zz}$  (Figure 3). This evolution is consistent with previous digital volume correlation analyses of X-ray tomogram triaxial compression experiments (Renard et al., 2019, McBeck et al., 2019, 2020c). The observed increase of the local, incremental dilation with increasing differential stress is also consistent with previous measurements of the macroscopic, cumulative volumetric strain of Westerly granite during triaxial compression (e.g., Brace et al., 1966, Bieniawski, 1967; Brace, 1978). In triaxial compression experiments on low porosity crystalline rocks, the macroscopic volumetric strain measured from the change in shape of the sample first evolves with the differential stress approximately linearly, with increasingly contractive values, or negative in the adopted sign convention. Then, at the onset of dilatancy, C', which may be about 50-75% of the stress at failure (Brace, 1978), the volumetric strain begins to develop increasingly dilative values, and the macroscopic dilation continually increases until macroscopic failure. The progressive

increase of the macroscopic dilation observed following C' in triaxial compression experiments is consistent with the observed acceleration of the volume of rock occupied by dilation observed in the present analysis.

Comparing the fraction of the rock core that hosts dilation immediately preceding failure among the experiments indicates that increasing  $\sigma_2$  generally promotes greater dilation (Figure 3). One may expect that greater  $\sigma_2$  would suppress dilation. Indeed, triaxial compression experiments on porous rocks such as Berea sandstone and Adamswiller sandstone show that when  $\sigma_2$  increases from 5 MPa to 40 MPa, the cumulative amount of inelastic dilation, which occurs following the onset of dilatancy and until macroscopic failure, decreases (Jamison & Teufel, 1979; Wong et al., 1997). However, for low porosity crystalline rocks, the relationship between  $\sigma_2$  and the dilation follows the opposite trend observed in the sandstone (e.g., Brace & Orange, 1968; Crouch, 1970; Paterson & Wong, 2005 p. 70), and the same trend observed in the present experiments. In particular, for Westerly granite and Witwatersrand quartzite, larger  $\sigma_2$  increases the inelastic dilation within the range of 3 to 30 MPa  $\sigma_2$  for the quartzite, and 160 to 500 MPa  $\sigma_2$  for the granite (Brace & Orange, 1968; Crouch, 1970). These results highlight a fundamental difference in the accumulation of dilatancy in low porosity crystalline rocks, in which fracture propagation and opening promotes dilatancy, and porous rocks, in which pore collapse and cataclasis may inhibit dilatancy.

To compare our results to this previous work, we calculate the amount of inelastic volumetric strain (dilation) that develops between the onset of dilatancy, C' (Brace, 1978), and macroscopic failure using the change in shape of the rock core observed in the X-ray tomograms (**Figure 11a, b**). We then compare these values to the sum of the volume fraction occupied by dilation, and the sum of the mean dilation from the onset of loading until failure calculated from the local incremental strains derived via digital volume correlation (**Figure 11c, d**). The identified values of C' are estimates based on the reversal in the slopes of the volumetric strain and differential stress curves. These estimates occur near 75% of the differential stress at failure, consistent with previous observations of the stress at C' (Brace, 1978).

Examining the macroscopic inelastic volumetric strain indicates that increasing  $\sigma_2$  generally promotes more inelastic dilation (**Figure 11b**). The two damaged experiments, WG06 and WG18, deviate from the overall trend of increasing inelastic dilation with increasing  $\sigma_2$ . These experiments produce more inelastic strain than expected from the intact experiments with the corresponding  $\sigma_2$ . Previous work shows that more preexisting damage generally produces longer macroscopic yielding phases in which more volumetric and axial strain accumulate. In particular, sandstone with some significant porosity accumulates more volumetric and axial strain than granite during triaxial compression (e.g., Feng et al., 2019). Examining the cumulative volume fraction of dilation also shows that the damaged experiments WG06 and WG18 host larger volume fractions of dilation than expected from the corresponding intact experiments (**Figure 11c**). In summary, the cumulative volume fraction (**Figure 11c**), the cumulative mean dilation (**Figure 11d**), and the macroscopic inelastic volumetric strain (**Figure 11b**) all suggest that larger  $\sigma_2$  promotes more dilation, consistent with previous measurements of low porosity crystalline rock (e.g., Brace & Orange, 1968; Crouch, 1970).

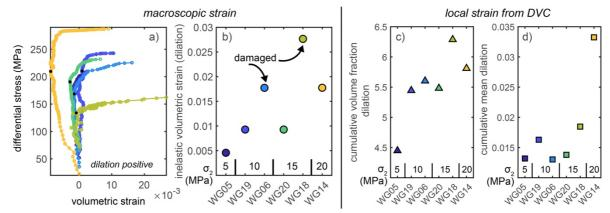


**Figure 11**. The influence of  $\sigma_2$  on dilatancy. Evolution of the volumetric strain calculated from the shape change of the rock core observed in the X-ray tomograms (a), the amount of inelastic volumetric strain between the onset of dilatancy, C', and macroscopic failure (b), and the cumulative volume fraction of the dilation (c) and cumulative mean dilation (d) calculated from the local strain derived from digital volume correlation. The black dots in (a) shows the location of C'. Increasing  $\sigma_2$  produces more dilation.

494 495

496 497

498

499

500

501

502

503

504

505

506

507

508

509

510

511

512

513

514

515516

517

518

519

520

521

522

523524

525526

527

528

529

530

### 4.2. The influence of confining stress on localization approaching macroscopic failure

Tracking the volume of the polyhedron that surrounds the high contraction, dilation and shear strain indicates that the high strain events localize approaching macroscopic failure in all three components for the vast majority of the experiments (Figure 5). However, for all the tested parameters, the dilation localizes approaching failure more often (80% of the combinations of parameters produce negative changes in volume) than the shear strain (67%) (e.g., Figure 6, Figure 7). This result is consistent with a previous analysis of the localization of the volumetric and shear strain in a different set of X-ray tomography experiments on Westerly granite, Fontainebleau sandstone, Mt. Etna basalt, Green River shale, and Anstrude limestone (McBeck et al., 2022b). In this previous analysis and the present analysis, the high magnitudes of the volumetric strains localize to a greater extent than the shear strain. In addition, in the present analysis, the maximum strain localization occurs immediately preceding failure for the dilation, on average at 0.98  $\widetilde{\epsilon_{zz}}$  for the intact rocks, but occurs earlier in loading for the shear strain, on average at 0.93  $\widetilde{\varepsilon_{zz}}$  for the intact rocks (**Figure 10**). Thus, the dilation hosts more systematic increases in localization towards failure than the shear strain, and the timing of maximum localization occurs almost exactly at macroscopic failure. Consequently, both the previous and present analyses suggest that the high magnitudes of the volumetric strains may provide more reliable information about the timing of catastrophic failure than the shear strain. Indeed, machine learning analyses indicate that the evolution of the dilative strain helps predict the timing of macroscopic failure in X-ray tomography experiments, and that the shear strain provides less useful information about the timing of failure (McBeck et al., 2020a). However, machine learning analyses of three-dimensional discrete element method numerical models of segmented fault networks within shear zones indicate that the shear strain provides more useful information about the timing of fault reactivation and macroscopic failure than the volumetric strain (McBeck et al., 2022a). Consequently, the utility of the volumetric strains for predicting the timing of failure may depend on the tectonic environment, and the existence of system-spanning, macroscopic faults.

Comparing the degree of localization near failure among the different experiments indicates that higher  $\sigma_2$  promotes greater localization approaching macroscopic failure

(Figure 5, Figure 6, Figure 7, Figures S2-S5). In the brittle portion of the crust, strike-slip faults tend to develop flower structures: a diffuse network of fractures near the surface that then localizes into a narrower zone at depth (Harding, 1985; Sylvester, 1988; Le Guerroue & Cobbold, 2006, Rockwell & Ben-Zion, 2007) (Figure 12a). This structure implies that increasing confining stress promotes localization. In addition, seismic observations indicate that low velocity zones surrounding large crustal faults, such as the San Jacinto fault (Wang et al., 2019), can narrow with depth. Moreover, low magnitude seismicity between large magnitude earthquakes in southern and Baja California increases in localization with increasing depth (Ben-Zion & Zaliapin, 2019). Such fault zones are the result of the accumulation of many cycles of fault growth, including coseismic slip and precursory localization. Here, we show that in one cycle of precursory deformation leading to macroscopic failure, greater confining stress leads to greater localization of the high strain events.

Observations of post-mortem fracture networks that form in uniaxial and triaxial compression experiments support the idea that increasing confining stress promotes localization (e.g., Paterson, 1958; Paterson & Wong, 2005 p. 212). Under uniaxial compression and low confining stresses in triaxial compression, rock cores fail by axial splitting, in which arrays of fractures aligned parallel to the maximum compression direction develop (e.g., **Figure 12b**). These fracture networks are often diffusely distributed, with several fractures extending from the top to the bottom of the core (e.g., Akdag et al., 2021; Basu et al. 2013; Hu et al., 2021). Under higher confining stresses, the rock cores fail through the development of one or a few macroscopic shear fractures, perhaps as a pair as conjugate shear fractures (e.g., Paterson, 1958; Lee & Rathnaweera, 2016). Although these fractures may develop from the coalescence of many small fractures, the final fracture geometry identified following the maximum stress consists of a few system-spanning fractures. Consequently, the fracture geometries that develop under uniaxial compression and low confining stress tend to be less localized than the fracture geometries that develop at higher confining stresses.

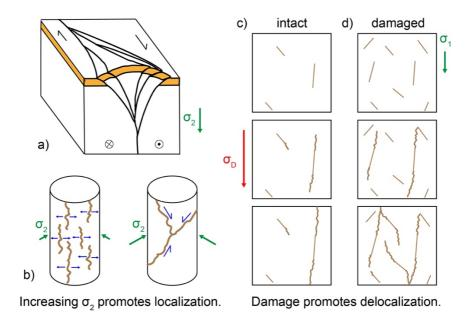


**Figure 12.** Examples of increasing confining stress promoting localization (a-b), and preexisting damage promoting delocalization (c-d). a) Positive flower structures that develop along strike-slip fault networks host a diffuse network of fractures at the surface that localize

into a narrower zone with depth. b) The tensile-dominated fracture networks that develop under low confining stress or uniaxial compression tend to be more diffusely spread (left) than the shear-dominated fracture networks that coalesce under higher confining stress (right). c) With lower amounts of preexisting damage, only a few of the longest and most favorably oriented fractures grow under increasing differential stress. d) With more preexisting damage, several of the smaller fractures may grow, rather than the few longest fractures, thereby producing delocalization.

 A network of fractures dominated by shear may be more localized than a network dominated by tension because the stress concentrations that develop at preexisting fractures and heterogeneities may be more important for the coalescence of shear fractures than the propagation of extensile fractures. Because the tensile strength of rocks is lower than the shear strength (Paterson & Wong, 2005 p. 22), extensile fractures may more easily develop throughout the rock core than shear fractures. Shear fractures may thus depend on the stress concentrations that develop near preexisting fractures in order to propagate and coalesce to a greater extent than the extensile fractures. Consequently, the shear fractures may be more likely to develop near preexisting fractures than the extensile fractures, producing more localized fault networks. Consistent with these theoretical arguments, laboratory observations, and crustal observations of fault structures at depth, the present analysis shows that increasing confining stress promotes greater increases in localization of the high strain events approaching macroscopic failure.

# 4.3. The influence of preexisting damage on localization approaching macroscopic failure

The present analysis shows that rocks can experience temporary episodes of delocalization, rather than a continuous increase or acceleration of localization toward catastrophic failure (e.g., **Figure 5**). This result is consistent with previous analyses of fracture development (McBeck et al., 2021a) and strain localization (McBeck et al., 2022b) in X-ray tomography triaxial compression experiments. This previous analysis found that the maximum strain localization generally occurs near 90% of the differential stress at macroscopic failure, rather than at macroscopic failure (McBeck et al., 2022b). In particular, only 46% of the experiments achieve maximum localization at macroscopic failure, or >99% of the failure stress. These results are similar to the damaged rocks in present analysis. For the damaged rocks, the maximum strain localization occurs on average at 94% (contraction), 86% (dilation), and 90% (shear strain) of the differential stress at failure. In contrast, for the intact rocks, the maximum strain localization occurs immediately preceding failure, and on average at 99% (contraction and dilation), and 95% (shear strain) of the differential stress at failure (**Figure 10**).

The results of the previous analysis (McBeck et al., 2022b) may be more consistent with the results of the damaged Westerly granite than the intact Westerly granite because the majority of the experiments used in the previous analysis were performed on rocks with more preexisting pores and fractures than the intact Westerly granite, such as Fontainebleau sandstone and Mt. Etna basalt. The localization behavior of sandstone and basalt is expected to be more similar to damaged Westerly granite than intact Westerly granite because the presence of preexisting damage can influence fracture development (e.g., Helgeson & Aydin, 1991; Tang et al., 2000; d'Alession & Martel, 2004; Gudmundsson et al., 2010; Cartwright-Taylor et al., 2020; Vasseur et al., 2015), and deformation localization (McBeck et al. 2021b). For example, analyses of fracture development in numerical models show that more heterogeneous models produce more precursors than less heterogeneous models (Tang et al., 2000). The precursors in the more heterogeneous models develop in a diffuse distribution

early in loading, and then coalesce into a system-spanning fracture that ultimately causes macroscopic failure. In contrast, in less heterogeneous models, only a few precursors develop at random positions throughout the rock, and these positions do not help indicate the final geometry of the system-spanning fracture that causes macroscopic failure. These numerical results are consistent with observations of fracture network development in X-ray tomography triaxial compression experiments on nominally intact and heat-treated (damaged) Ailsa Craig microgranite (Cartwright-Taylor et al., 2020). These experiments show that the heat-treated, and thus more heterogeneous, rock develops more precursory fractures throughout loading toward failure, producing a smooth, continuous evolution, indicative of a second-order transition (Cartwright-Taylor et al., 2020). In contrast, the nominally intact rock hosts few detectable precursors preceding macroscopic failure, producing an abrupt, or firstorder, transition. Similarly, numerical models of strike-slip faults embedded in host rock with varying amounts of preexisting weaknesses show that the fracture networks in more homogeneous models continually increase in localization toward macroscopic failure (McBeck et al., 2021b). In contrast, more heterogeneous models experience phases of delocalization superposed on the overall trend of increasing localization. Observations of low-magnitude seismicity preceding several M>7 earthquakes in Southern and Baja California reveal similar phases of delocalization (Ben-Zion & Zaliapin, 2020).

Consistent with the observed influence of heterogeneities on fracture development and localization, the present analysis shows that the damaged Westerly granite experiences maximum localization earlier in loading than the intact Westerly granite (**Figure 10**). Moreover, the proportion of the macroscopic axial strain in which the intact rocks experience localization is larger than the proportion in which the damaged rocks experience localization (**Figure 9**). In addition, the intact rocks tend to experience more cumulative localization throughout loading (**Figure 6**), greater increases in localization immediately preceding failure (**Figure 7**), and smaller v and thus greater absolute localization at failure (**Figure S4**) than the damaged rocks. Thus, more preexisting damage favors delocalization.

The damaged rocks, and more heterogeneous systems in general, may promote episodes of delocalization because the stress concentrations that develop at heterogeneities may allow fracture propagation to require less energy in a network with many smaller fractures than in a more sparsely populated fracture network with several large fractures and only a few smaller fractures (e.g., **Figure 11c**). This effect produces the decreasing strength of rocks at increasing length-scales (e.g., Lockner, 1995; Paterson & Wong, 2005 p. 31). Because larger rock volumes are more likely to contain longer fractures than smaller rock volumes, these longer fractures develop stress concentrations that trigger fracture propagation, and ultimately produce macroscopic failure at a lower level of stress than smaller rock volumes. Consequently, the existence of a diffuse network of heterogeneities enables propagation from many smaller fractures that may delocalize the overall deformation away from the few largest fractures. A diffuse fracture network would also provide a greater opportunity for stress shadows to inhibit growth between fractures (e.g., Nur, 1982) than a more clustered network, and thereby promote delocalization.

### 5 Conclusions

To assess the influence of confining stress and preexisting damage on strain localization, we perform a series of X-ray tomography triaxial compression experiments on Westerly granite, and then use digital volume correlation to estimate the local three-dimensional strain tensors throughout loading until macroscopic failure. We examine the evolving volume of the polyhedron that surrounds the highest values of three strain

657 components: the contraction, dilation, and shear strain. We find that experiments with higher confining stress (>10 MPa) host larger amounts of dilation than experiments with lower 658 confining stress, consistent with previous laboratory analyses on low porosity crystalline rock 659 660 (e.g., Brace & Orange, 1968; Crouch, 1970). Higher confining stress is also associated with larger increases in localization of the high strain events approaching macroscopic failure. 661 This positive correlation between confining stress and localization is consistent with the 662 663 localized geometry of the shear-dominated fractures that develop at higher confining stresses 664 compared to the more diffuse arrangement of the extensile-dominated fractures that develop in uniaxial compression (e.g., Paterson, 1958), and with crustal observations of strike-slip 665 666 fault networks that narrow with depth (e.g., Sylvester, 1988; Rockwell & Ben-Zion, 2007). Tracking the volume of the high strains shows that the strain events do not always 667 systematically increase in localization towards failure, but instead experience phases of 668 delocalization. This result is consistent with previous X-ray tomography triaxial compression 669 experiments (McBeck et al., 2021a; McBeck et al., 2022b), and with observations of low 670 magnitude seismicity in Southern and Baja California (Ben-Zion & Zaliapin, 2020). The 671 672 amount of preexisting damage controls the extent of the phases of delocalization, and when the rock experiences the greatest localization of the high strain events. The damaged rocks 673 674 experience longer proportions of the experiment time, in terms of the macroscopic axial 675 strain, in which the strains are delocalizing than the intact rocks. The heat-treated, and thus 676 damaged, Westerly granite experiments host the greatest localization of the high strain events 677 on average near 90% of the differential stress at failure, consistent with strain localization in 678 rocks with some preexisting porosity and heterogeneities, such as Mt. Etna basalt and Fontainebleau sandstone (McBeck et al., 2022b). In contrast, the intact Westerly granite 679 680 experiments host the greatest localization of the high strain events on average near 99% of the differential stress at failure. In addition, the high strain events localize by larger 681 682 magnitudes preceding failure in the intact rocks than the damaged rocks. Consequently, more preexisting damage favors delocalization. More preexisting damage may allow more 683 684 delocalization because the stress concentrations that develop at preexisting heterogeneities 685 periodically enable smaller fractures to propagate, and form stress shadows that inhibit growth. The results show that the dilation hosts more systematic increases in localization 686 687 towards failure than the shear strain, consistent with a previous digital volume correlation 688 analysis (McBeck et al., 2022b), and that the timing of maximum localization occurs almost exactly at macroscopic failure, consistent with a machine learning analysis that found that the 689 690 dilative strain helps predict the timing of catastrophic failure better than the shear strain 691 (McBeck et al., 2020a). Consequently, the dilative strain may provide more reliable 692 information about the timing of catastrophic failure than the shear strain.

# Acknowledgements

693

700

- The Research Council of Norway (grant 300435 to JM), U.S. National Science Foundation
- 695 (grant EAR-2122168 to YBZ) and the European Research Council under the European
- Union's Horizon 2020 research and innovation program (grant No. 101019628 BREAK to
- 697 FR) funded this work. Beamtime was allocated at the European Synchrotron Radiation
- 698 Facility (Long Term Proposal ES-1190). We thank Clémence Muzelle for technical support
- on beamline ID19 at ESRF.

# Open Research

- 701 The experimental data (time series of X-ray tomograms) are available on Norstore with DOI
- 702 10.11582/2023.00007
- 703 (https://archive.norstore.no/pages/public/datasetDetail.jsf?id=10.11582/2023.00007).

### 704 References

- Akdag, S., Karakus, M., Nguyen, G. D., Taheri, A., & Bruning, T. (2021). Evaluation of the
- propensity of strain burst in brittle granite based on post-peak energy analysis. Underground
- 707 Space, 6(1), 1-11.
- 708 Basu, A., Mishra, D. A., & Roychowdhury, K. (2013). Rock failure modes under uniaxial
- 709 compression, Brazilian, and point load tests. Bulletin of Engineering Geology and the
- 710 Environment, 72, 457-475.
- 711 Ben-Zion, Y. and I. Zaliapin, (2019). Spatial variations of rock damage production by
- earthquakes in southern California, Earth and Planetary Science Letters, 512, 184–193.
- 713 Ben-Zion, Y., & Zaliapin, I. (2020). Localization and coalescence of seismicity before large
- earthquakes. Geophysical Journal International, 223(1), 561-583.
- 715 Benson, P. M., Thompson, B. D., Meredith, P. G., Vinciguerra, S., & Young, R. P. (2007).
- 716 Imaging slow failure in triaxially deformed Etna basalt using 3D acoustic-emission location
- and X-ray computed tomography. Geophysical Research Letters, 34(3), L03303.
- 718 Bieniawski, Z. T. (1967). Mechanism of brittle fracture of rock: Part I. Theory of the fracture
- 719 process. Part II. Experimental studies; Part III. Fracture in tension and under long-term
- 720 loading. International Journal of Rock Mechanics and Mining Sciences & Geomechanics
- 721 Abstracts, 4(4), 395-406.
- 722 Brace, W. F. (1978). Volume changes during fracture and frictional sliding: A review. Pure
- 723 and Applied Geophysics, 116, 603-614.
- Prace, W. F., & Orange, A. S. (1968). Electrical resistivity changes in saturated rocks during
- fracture and frictional sliding. Journal of Geophysical Research, 73(4), 1433-1445.
- 726 Brace, W. F., Paulding Jr, B. W., & Scholz, C. H. (1966). Dilatancy in the fracture of
- 727 crystalline rocks. Journal of Geophysical Research, 71(16), 3939-3953.
- Buades, A., Coll, B., & Morel, J. M. (2005). A non-local algorithm for image denoising. In
- 729 2005 IEEE Computer Society Conference on Computer Vision and Pattern Recognition
- 730 (CVPR'05), 2, 60-65.
- 731 Cartwright-Taylor, A., Main, I. G., Butler, I. B., Fusseis, F., Flynn, M., & King, A. (2020).
- 732 Catastrophic failure: how and when? Insights from 4-D in situ x-ray microtomography.
- Journal of Geophysical Research: Solid Earth, 125(8), e2020JB019642.
- Charalampidou, E. M., Hall, S. A., Stanchits, S., Lewis, H., & Viggiani, G. (2011).
- 735 Characterization of shear and compaction bands in a porous sandstone deformed under
- 736 triaxial compression. Tectonophysics, 503(1-2), 8-17.
- 737 Crouch, S. L. (1970). Experimental determination of volumetric strains in failed rock. In
- 738 International Journal of Rock Mechanics and Mining Sciences & Geomechanics Abstracts,
- 739 7(6), 589-603.
- 740 d'Alessio, M. A., & Martel, S. J. (2004). Fault terminations and barriers to fault growth.
- 741 Journal of Structural Geology, 26(10), 1885-1896.
- Feng, X. T., Kong, R., Zhang, X., & Yang, C. (2019). Experimental study of failure
- 743 differences in hard rock under true triaxial compression. Rock Mechanics and Rock
- 744 Engineering, 52, 2109-2122.
- 745 Fredrich, J. T., & Wong, T. F. (1986). Micromechanics of thermally induced cracking in
- three crustal rocks. Journal of Geophysical Research: Solid Earth, 91(B12), 12743-12764.

- Griffiths, L., Heap, M. J., Baud, P., & Schmittbuhl, J. (2017). Quantification of microcrack
- characteristics and implications for stiffness and strength of granite. International Journal of
- Rock Mechanics and Mining Sciences, 100, 138-150.
- Gudmundsson, A., Simmenes, T. H., Larsen, B., & Philipp, S. L. (2010). Effects of internal
- structure and local stresses on fracture propagation, deflection, and arrest in fault zones.
- 752 Journal of Structural Geology, 32(11), 1643-1655.
- Gueydan, F., Précigout, J., & Montesi, L. G. (2014). Strain weakening enables continental
- 754 plate tectonics. Tectonophysics, 631, 189-196.
- Harding, T. P. (1985). Seismic characteristics and identification of negative flower structures,
- positive flower structures, and positive structural inversion. AAPG bulletin, 69(4), 582-600.
- 757 Helgeson, D. E., & Aydin, A. (1991). Characteristics of joint propagation across layer
- interfaces in sedimentary rocks. Journal of Structural Geology, 13(8), 897-911.
- 759 Hu, J., Zeng, P., Yang, D., Wen, G., Xu, X., Ma, S., Zhao, F., & Xiang, R. (2021).
- 760 Experimental investigation on uniaxial compression mechanical behavior and damage
- evolution of pre-damaged granite after cyclic loading. Energies, 14(19), 6179.
- Jamison, W. R., & Teufel, L. W. (1979). Pore volume changes associated with failure and
- 763 frictional sliding of a porous sandstone. 20th US Symposium on Rock Mechanics (USRMS).
- 764 OnePetro.
- Le Guerroué, E., & Cobbold, P. R. (2006). Influence of erosion and sedimentation on strike-
- slip fault systems: insights from analogue models. Journal of Structural Geology, 28(3), 421-
- 767 430.
- Lee, B., & Rathnaweera, T. D. (2016). Stress threshold identification of progressive
- 769 fracturing in Bukit Timah granite under uniaxial and triaxial stress conditions. Geomechanics
- and Geophysics for Geo-Energy and Geo-Resources, 2, 301-330.
- Lockner, D. A. (1995). Rock failure: Rock Physics and Phase Relations. A Handbook of
- Physical Constants. Am. Geophys. Union Reference Shelf. Am. Geophys. Union, 127-141.
- Lockner, D., Byerlee, J. D., Kuksenko, V., Ponomarev, A., & Sidorin, A. (1991). Quasi-static
- fault growth and shear fracture energy in granite. Nature, 350(6313), 39-42.
- 775 Lyakhovsky, V., Hamiel, Y., & Ben-Zion, Y. (2011). A non-local visco-elastic damage
- model and dynamic fracturing. Journal of the Mechanics and Physics of Solids, 59(9), 1752-
- 777 1776.
- McBeck, J., Aiken, J. M., Ben-Zion, Y., & Renard, F. (2020a). Predicting the proximity to
- 779 macroscopic failure using local strain populations from dynamic in situ X-ray tomography
- triaxial compression experiments on rocks. Earth and Planetary Science Letters, 543, 116344.
- 781 McBeck, J. A., Aiken, J. M., Mathiesen, J., Ben-Zion, Y., & Renard, F. (2020b). Deformation
- 782 precursors to catastrophic failure in rocks. Geophysical Research Letters, 47(24),
- 783 e2020GL090255.
- McBeck, J., Ben-Zion, Y., & Renard, F. (2020c). The mixology of precursory strain
- partitioning approaching brittle failure in rocks. Geophysical Journal International, 221(3),
- 786 1856-1872.
- 787 McBeck, J., Ben-Zion, Y., & Renard, F. (2021a). Fracture network localization preceding
- catastrophic failure in triaxial compression experiments on rocks. Frontiers in Earth Science,
- 789 9, 778811.

- 790 McBeck, J., Ben-Zion, Y., & Renard, F. (2022a). Predicting fault reactivation and
- 791 macroscopic failure in discrete element method simulations of restraining and releasing step
- 792 overs. Earth and Planetary Science Letters, 593, 117667.
- 793 McBeck, J., Ben-Zion, Y., & Renard, F. (2022b). Volumetric and shear strain localization
- throughout triaxial compression experiments on rocks. Tectonophysics, 822, 229181.
- McBeck, J., Ben-Zion, Y., Zhou, X., & Renard, F. (2021b). The influence of preexisting host
- rock damage on fault network localization. Journal of Structural Geology, 153, 104471.
- 797 McBeck, J. A., Cordonnier, B., Vinciguerra, S., & Renard, F. (2019). Volumetric and shear
- strain localization in Mt. Etna basalt. Geophysical Research Letters, 46(5), 2425-2433.
- 799 McBeck, J., Kobchenko, M., Hall, S. A., Tudisco, E., Cordonnier, B., Meakin, P., & Renard,
- 800 F. (2018). Investigating the onset of strain localization within anisotropic shale using digital
- volume correlation of time-resolved X-ray microtomography images. Journal of Geophysical
- 802 Research: Solid Earth, 123(9), 7509-7528.
- 803 Mulyukova, E., & Bercovici, D. (2019). The generation of plate tectonics from grains to
- global scales: A brief review. Tectonics, 38(12), 4058-4076.
- Nur, A. (1982). The origin of tensile fracture lineaments. Journal of Structural Geology, 4(1),
- 806 31-40.
- Paterson, M. S. (1958). Experimental deformation and faulting in Wombeyan marble.
- 808 Geological Society of America Bulletin, 69(4), 465-476.
- Paterson, M. S., & Wong, T. F. (2005). Experimental rock deformation: the brittle field, 348.
- 810 Berlin: Springer.
- Renard, F., Cordonnier, B., Dysthe, D. K., Boller, E., Tafforeau, P., & Rack, A. (2016). A
- deformation rig for synchrotron microtomography studies of geomaterials under conditions
- down to 10 km depth in the Earth. Journal of Synchrotron Radiation, 23(4), 1030-1034.
- Renard, F., McBeck, J., Kandula, N., Cordonnier, B., Meakin, P., & Ben-Zion, Y. (2019).
- Volumetric and shear processes in crystalline rock approaching faulting. Proceedings of the
- 816 National Academy of Sciences, 116(33), 16234-16239.
- 817 Rockwell, T. K., & Ben-Zion, Y. (2007). High localization of primary slip zones in large
- 818 earthquakes from paleoseismic trenches: Observations and implications for earthquake
- physics. Journal of Geophysical Research: Solid Earth, 112(B10).
- Rudnicki, J. W., & Rice, J. R. (1975). Conditions for the localization of deformation in
- pressure-sensitive dilatant materials. Journal of the Mechanics and Physics of Solids, 23(6),
- 822 371-394.
- 823 Satoh, T., Shivakumar, K., Nishizawa, O., & Kusunose, K. (1996). Precursory localization
- and development of microfractures along the ultimate fracture plane in amphibolite under
- triaxial creep. Geophysical Research Letters, 23(8), 865-868.
- 826 Sylvester, A. G. (1988). Strike-slip faults. Geological Society of America Bulletin, 100(11),
- 827 1666-1703.
- 828 Tang, C. A., Liu, H., Lee, P. K. K., Tsui, Y., & Tham, L. (2000). Numerical studies of the
- influence of microstructure on rock failure in uniaxial compression—part I: effect of
- heterogeneity. International Journal of Rock Mechanics and Mining Sciences, 37(4), 555-
- 831 569.

### manuscript submitted to JGR Solid Earth

- 832 Tudisco, E., Andò, E., Cailletaud, R., & Hall, S. A. (2017). TomoWarp2: A local digital
- volume correlation code. SoftwareX, 6, 267-270.
- Vasseur, J., Wadsworth, F. B., Lavallée, Y., Bell, A. F., Main, I. G., & Dingwell, D. B.
- 835 (2015). Heterogeneity: The key to failure forecasting. Scientific Reports, 5(1), 13259.
- Wang, Y., Allam, A., & Lin, F. C. (2019). Imaging the fault damage zone of the San Jacinto
- fault near Anza with ambient noise tomography using a dense nodal array. Geophysical
- 838 Research Letters, 46(22), 12938-12948.
- Wong, T. F., David, C., & Zhu, W. (1997). The transition from brittle faulting to cataclastic
- 840 flow in porous sandstones: Mechanical deformation. Journal of Geophysical Research: Solid
- 841 Earth, 102(B2), 3009-3025.



JGR: Solid Earth

### Supporting information for:

The influence of confining stress and preexisting damage on strain localization in fluid-saturated crystalline rocks at the stress conditions of the upper crust

## Jessica McBeck<sup>1</sup>, Benoît Cordonnier<sup>2</sup>, Yehuda Ben-Zion<sup>3</sup>, François Renard<sup>1,4</sup>

<sup>1</sup>Njord Centre, Departments of Physics and Geosciences, University of Oslo, Oslo, Norway.

<sup>3</sup>Department of Earth Sciences and Southern California Earthquake Center, University of Southern California, Los Angeles, CA, USA.

<sup>4</sup>Université Grenoble Alpes, Université Savoie Mont Blanc, Université Gustave Eiffel, CNRS, IRD, ISTerre, 38000 Grenoble, France.

### **Contents of this file**

Figures S1 to S5 Table S1

<sup>&</sup>lt;sup>2</sup>European Synchrotron Radiation Facility, Grenoble, France

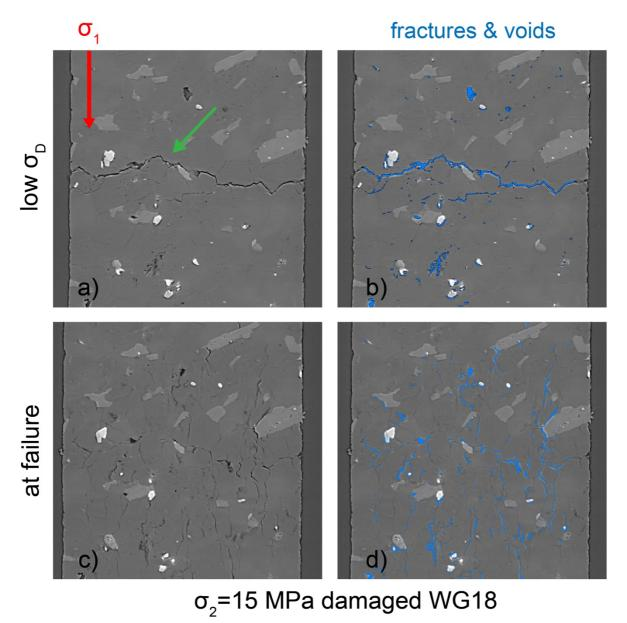


**Figure S1**. Two-dimensional slices of the tomograms (a, c) and segmented voids and fractures (b, d) in experiment WG18 at lower differential stress,  $\sigma_D$  (a, b), and higher  $\sigma_D$ , immediately preceding macroscopic failure (c, d). This rock core developed a horizontal, core-spanning fracture as it was loaded into the triaxial deformation apparatus, highlighted with a green arrow in (a). With increasing axial and differential stress the fracture closed, producing arrays of mostly vertically-aligned fractures that grew until system-size failure.

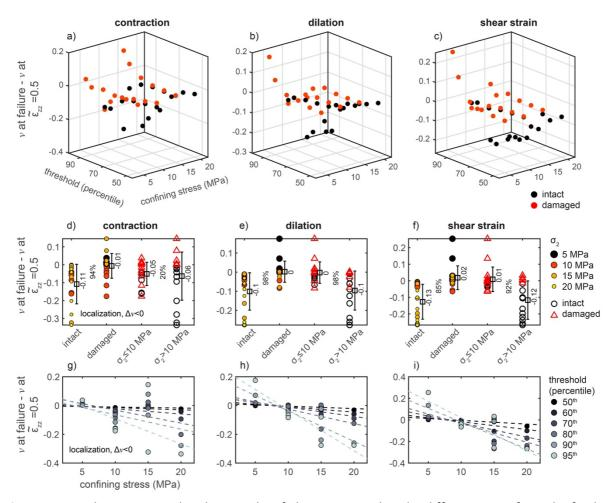


**Figure S2**. Localization immediately preceding failure measured as the difference in v from the final tomogram acquired immediately preceding failure, when  $\widetilde{\varepsilon_{zz}}$  is one, and when  $\widetilde{\varepsilon_{zz}}$  is 0.5,  $\Delta v$ . Negative  $\Delta v$  indicates that the high strain events localize towards macroscopic failure. The format of the figure is the same as **Figure 6**.

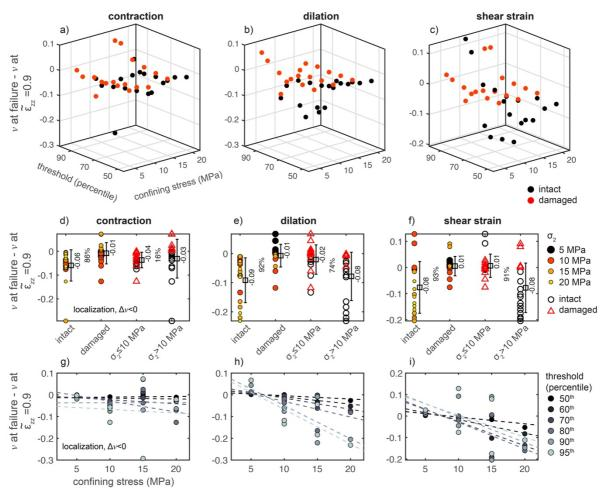


**Figure S3**. Localization immediately preceding failure measured as the difference in v from the final tomogram acquired immediately preceding failure, when  $\widetilde{\varepsilon_{zz}}$  is one, and when  $\widetilde{\varepsilon_{zz}}$  is 0.9,  $\Delta v$ . Negative  $\Delta v$  indicates that the high strain events localize towards macroscopic failure. The format of the figure is the same as **Figure 6**.

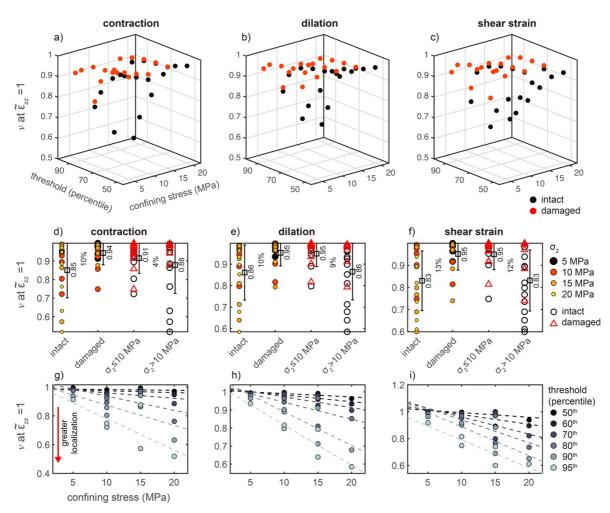


**Figure S4**. The spatial clustering, v, of the high strain events immediately preceding failure, when  $\widetilde{\varepsilon_{zz}}$  is one. Format is the same as **Figure 6**. The trends shown here are similar to those observed for the cumulative localization (**Figure 6**), and localization from when  $\widetilde{\varepsilon_{zz}}$  is 0.5, 0.8 or 0.9, to macroscopic failure (**Figures S2-S3**).

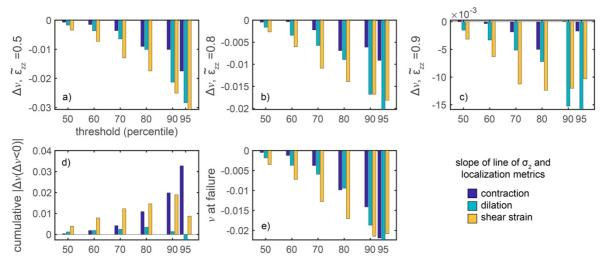


**Figure S5**. Slopes of the linear fit of different localization metrics for strains >90<sup>th</sup> percentile and  $\sigma_2$  of the experiments for each strain component: contraction (dark blue), dilation (light blue), and shear strain (yellow). The horizontal axis indicates strain threshold used to calculate the slope. Each plot shows the slopes for different localization metrics: a-c)  $\Delta v$  using  $\widetilde{\varepsilon_{zz}}$ =0.5,  $\widetilde{\varepsilon_{zz}}$ =0.8, and  $\widetilde{\varepsilon_{zz}}$ =0.9,

d) the cumulative localization, and e) v at failure. Larger magnitudes indicate a stronger influence of  $\sigma_2$  on localization. The lines that produce each slope are shown in **Figure** 6, **Figure** 7, **Figure** S2, **Figure** S3, and **Figure** S4.

The confining stress	$\sigma_2$
The fluid pressure	$P_F$
The effective stress, $\sigma_2 - P_f$	$P_e$
The macroscopic cumulative axial strain measured from the change in height of	$\mathcal{E}_{ZZ}$
the rock core observed in the tomogram	
The normalized $\varepsilon_{zz}$ . $\widetilde{\varepsilon_{zz}}$ is calculated from the $\varepsilon_{zz}$ calculated for the given	$\widetilde{arepsilon_{zz}}$
tomogram, the $arepsilon_{zz}$ of the tomogram acquired immediately preceding	
macroscopic failure, $\varepsilon_{zz}^F$ , and the $\varepsilon_{zz}$ of the first tomogram acquired at the onset	
of the linear phase early in loading, $\varepsilon_{zz}^0$ , as $\widetilde{\varepsilon_{zz}} = (\varepsilon_{zz} - \varepsilon_{zz}^0)/(\varepsilon_{zz}^F - \varepsilon_{zz}^0)$	
The divergence of the incremental displacement field, the volumetric strain.	I1
Negative is contractive and positive is dilative.	
The second invariant of the deviatoric strain tensor derived from the	J2
displacement field, indicative of shear strain.	
The volume of the polyhedron that surrounds high values of each strain	$v_h$
component	
The volume of the polyhedron that surrounds all of the values of the given strain	$v_t$
component	
The volume proportion occupied by high strain events, $v = v_h/v_t$	v
The absolute value of the sum of the negative values of the change in $v$ from one	Cumulative
digital volume correlation calculation to the next, when $\widetilde{\varepsilon_{zz}}$ >0.5,	localization
$\sum_{\widetilde{\varepsilon_{zz}}=0.5}^{\widetilde{\varepsilon_{zz}}=1}  \Delta v(\Delta v < 0) $ . Increasing values indicate higher magnitudes of	
localization.	
Change in $v$ from DVC calculation $n$ +1 to $n$ , as $v_{n+1}-v_n$ , or change in $v$ from	$\Delta v$
$\widetilde{\varepsilon_{zz}}$ =1 to an earlier $\widetilde{\varepsilon_{zz}}$ , such as 0.5, 0.8, or 0.9. Negative $\Delta v$ indicates localization	
towards macroscopic failure.	

 Table S1. Symbols and notation used in the manuscript.